ORIGINAL ARTICLE

Extremes of summer Arctic sea ice reduction investigated with a rare event algorithm

Jerome Sauer[1] · Jonathan Demaeyer[2] · Giuseppe Zappa[3] · François Massonnet[1] · Francesco Ragone[1,2]

Abstract
Various studies identified possible drivers of extremes of Arctic sea ice reduction, such as observed in the summers of 2007 and 2012, including preconditioning, local feedback mechanisms, oceanic heat transport and the synoptic- and large-scale atmospheric circulations. However, a robust quantitative statistical analysis of extremes of sea ice reduction is hindered by the small number of events that can be sampled in observations and numerical simulations with computationally expensive climate models. Recent studies tackled the problem of sampling climate extremes by using rare event algorithms, i.e., computational techniques developed in statistical physics to reduce the computational cost required to sample rare events in numerical simulations. Here we apply a rare event algorithm to ensemble simulations with the intermediate complexity coupled climate model PlaSim-LSG to investigate extreme negative summer pan-Arctic sea ice area anomalies under pre-industrial greenhouse gas conditions. Owing to the algorithm, we estimate return times of extremes orders of magnitude larger than feasible with direct sampling, and we compute statistically significant composite maps of dynamical quantities conditional on the occurrence of these extremes. We find that extremely low sea ice summers in PlaSim-LSG are associated with preconditioning through the winter sea ice-ocean state, with enhanced downward longwave radiation due to an anomalously moist and warm spring Arctic atmosphere and with enhanced downward sensible heat fluxes during the spring-summer transition. As a consequence of these three processes, the sea ice-albedo feedback becomes active in spring and leads to an amplification of pre-existing sea ice area anomalies during summer.

Keywords Rare event algorithms · Climate extremes · Arctic sea ice variability · Climate model · EMIC

1 Introduction

The Arctic sea ice cover has been shrinking since at least the late 1970s (Notz and Marotzke 2012; Stroeve and Notz 2018), in large part due to anthropogenic emissions of greenhouse gases (Gregory et al. 2002; Notz and Marotzke 2012; Stroeve and Notz 2018; Ding et al. 2017). On top of the downward trend, internal climate variability contributes to the year-to-year variations and associated extreme events of the annual sea ice minimum in September (Francis and Wu 2020; Ono et al. 2019).

Extreme Arctic sea ice reduction, such as observed in the summers of 2007 and 2012, may have impacts outside the Arctic Ocean. Studies have suggested a possible influence of sea ice loss on the integrity of the permafrost (Lawrence et al. 2008) and on weather patterns and climate in the mid to high latitudes (Petoukhov and Semenov 2010; Francis et al. 2009; Francis and Vavrus 2012; Screen et al. 2018; Petrie et al. 2015; Chripko et al. 2021; Delhaye et al. 2022). Apart from its effect on the climate system, Arctic sea ice decline leads to increased marine accessibility. This has implications for the opening of trans-Arctic shipping routes, offshore industries, polar ecotourism and the daily life of local communities (Eicken 2013; Smith and Stephenson 2013; Lloyd's 2012).

Possible drivers of extreme summer Arctic sea ice reduction have been suggested in the literature. Both the extreme sea ice lows in 2007 and 2012 were attributed to climate

✉ Jerome Sauer
  jerome.sauer@uclouvain.be

1   Earth and Climate Research Center, Earth and Life Institute,
    Université catholique de Louvain, Louvain-la-Neuve,
    Belgium

2   Royal Meteorological Institute of Belgium, Brussels,
    Belgium

3   Institute of Atmospheric Sciences and Climate, National
    Research Council of Italy, Bologna, Italy

change via preconditioning through the ongoing winter sea ice thinning and to the occurrence of particular weather and climate events (Lindsay et al. 2009; Kauker et al. 2009; Zhang et al. 2008, 2013; Parkinson and Comiso 2013). In 2007, sea ice reduction was favoured by enhanced inflow of warm Pacific water through Bering Strait (Woodgate et al. 2010) and by anomalously persistent southerly winds in the Pacific sector associated with the Arctic Dipole (AD) pattern (Wang et al. 2009; Lindsay et al. 2009; Overland et al. 2012; Kauker et al. 2009). In 2012, a summer storm contributed to enhanced sea ice reduction by leading to increased bottom melt via anomalously strong vertical mixing in the oceanic boundary layer (Guemas et al. 2013; Zhang et al. 2013). Further possible triggers of anomalously low summer Arctic sea ice area include enhanced North Atlantic oceanic heat transport (Årthun et al. 2012), the positive and negative phases of the winter and summer Arctic Oscillation (AO) (e.g. Rigor et al. 2002; Ogi et al. 2016), reduced cloudiness during summer (Schweiger et al. 2008), and increased surface downward longwave radiation related to enhanced poleward atmospheric moisture transport during spring (Kapsch et al. 2013, 2019).

Even though different physical drivers have been suggested to contribute to individual extremes of Arctic sea ice reduction, a quantitative statistical analysis of their physical drivers is hindered by the poor sampling of extreme events in observations and in numerical simulations. The record of satellite-based sea ice observations includes only a few annual sea ice minima with orders of magnitude comparable to the ones in September 2007 and 2012 (Fetterer et al. 2017). Moreover, the large computational cost of state-of-the-art general circulation models makes it unrealistic to run them longer than a few thousands of years and to quantitatively study sea ice extremes with return times of longer than order 10^2 years. Going beyond individual case studies, a generalized analysis of the relative importance of different atmospheric and oceanic precursors of extremes of sea ice reduction remains therefore a challenge. A better understanding of the precursors of extremes of summer Arctic sea ice reduction and a more precise estimate of their probabilities are in turn crucial to improve seasonal predictions of these events and to assess their risk of occurrence under different climate change scenarios.

In this work, we address the problem of computational cost limitations by using a rare event algorithm. Rare event algorithms are computational techniques developed in statistical physics to improve the sampling efficiency of rare events in numerical simulations (e.g. Ragone et al. 2018; Ragone and Bouchet 2020, 2021). Compared to conventional numerical simulations with the same computational cost, rare event algorithms enable to increase the number of simulated extreme events by several orders of magnitude. In this way, these techniques allow to reduce the uncertainty of

return time estimates and of conditional statistics on extreme events (e.g. composites) compared to conventional simulation strategies, and to generate ultra-rare events that are very unlikely to be observed using direct sampling. Rare event algorithms have been introduced in the 1950s (Kahn and Harris 1951) and have been used since for a wide range of applications (for an overview and the mathematical analysis see e.g. Del Moral 2004; Giardina et al. 2011; Grafke and Vanden-Eijnden 2019). Recently, some of these techniques have been applied in climate science and in fluid dynamics to study heat waves (Ragone et al. 2018; Ragone and Bouchet 2020, 2021), midlatitude precipitation (Wouters et al. 2023), tropical storms (Plotkin et al. 2019; Webber et al. 2019), weakening and collapse of the Atlantic meridional overturning circulation (AMOC) (Cini et al. 2023), and turbulence (Bouchet et al. 2018; Grafke et al. 2015; Lestang et al. 2020).

Apart from rare event algorithms, other techniques exist that allow to study extreme events with return times beyond the range of available data. For example, extreme value theory (EVT) can be used to extrapolate return times for anomaly values unavailable from the data set (Coles 2001; Parey et al. 2010). EVT is used in climate science in particular for attribution studies, as it is an efficient way to estimate probabilities of events outside the range of observational data. However, one of the drawbacks is that it does not provide the dynamics that leads to the extrapolated extreme events. Moreover, a recently published approach to focus the computational power in climate model simulations on trajectories that lead to extreme events is ensemble boosting (Fischer et al. 2023; Gessner et al. 2023). In this approach, ensemble simulations are re-initialized days to weeks before the peak of an extreme event allowing to generate physically plausible ultra-rare events with unprecedented amplitude. Ensemble boosting thus allows to study the dynamics of unprecedented extreme events, but it does not provide the probabilities of these events and can therefore be used only in a story-line sense. Rare event algorithms instead deliver both the dynamical trajectories that lead to the extreme events of interest and enable to estimate their probabilities of occurrence. This allows for example to explore covariates of an observable of interest without the need of assumptions on the underlying distributions.

Different types of rare event algorithms are suited to study different problems, as the underlying design mechanisms are tailored to target extremes with specific properties. Here we use a genealogical selection algorithm (Ragone et al. 2018; Ragone and Bouchet 2020, 2021) adapted from Del Moral and Garnier (2005); Giardina et al. (2011), that is appropriate to study persistent, long lasting events. We apply this rare event algorithm to the intermediate complexity coupled climate model PlaSim-LSG (Fraedrich et al. 2005; Drijfhout et al. 1996; Maier-Reimer et al. 1993) to investigate extreme

negative summer pan-Arctic sea ice area anomalies under fixed pre-industrial greenhouse gas conditions. Owing to the algorithm, we compute return times two to three orders of magnitude larger than feasible with direct sampling and we obtain statistically significant composite maps of dynamical quantities conditional on the occurrence of extremely low sea ice summers with return times of more than 200 years. Finally, we elaborate possible physical drivers of these events. The paper is structured as follows. In Sect. 2, we present the set-up of the model and the control run and we describe the methodology of the rare event algorithm and the design of the rare event algorithm experiments. In Sect. 3, we show that the rare event algorithm performs importance sampling of summer seasons with extremely low pan-Arctic sea ice area and we discuss possible physical drivers of these events. In this context, we describe the average states of the atmosphere and of the sea ice during extremely low sea ice summers, we discuss the relative contribution of winter preconditoning vs. intra-seasonal sea ice reduction to extreme negative summer pan-Arctic sea ice area anomalies and we perform a surface energy budget analysis in order to trace back extremely low sea ice conditions to anomalous atmospheric conditions. In Sect. 4, we present our conclusions and we discuss possible future lines of research.

2 Materials and methods

2.1 The Planet Simulator with a Large-Scale Geostrophic ocean circulation model

All the following simulations are conducted with the intermediate complexity climate model Planet Simulator (PlaSim) version 17 (Fraedrich et al. 2005). To account for the importance of oceanic processes for Arctic sea ice variability, we use a coupled version of PlaSim that includes a dynamic Large-Scale Geostrophic (LSG) ocean (Maier-Reimer et al. 1993; Drijfhout et al. 1996) in addition to a mixed-layer ocean model and to a thermodynamic sea ice model (PlaSim coupled to LSG is referred to as "PlaSim-LSG" in this work). PlaSim-LSG is computationally less demanding than Earth system models used in the assessments of the Intergovernmental Panel on Climate Change (IPCC). It allows to conduct large ensemble simulations at reasonable computational cost, which is suitable for the aim of this work to investigate the applicability of a rare event algorithm to study extremes of Arctic sea ice reduction with a numerical climate model. Despite its intermediate complexity, PlaSim-LSG produces a reasonably realistic present-day climate, especially in the northern hemisphere (Angeloni 2022). Further applications for which PlaSim-LSG has been used include aquaplanet and paleoclimate studies (Hertwig et al. 2014; Andres and Tarasov 2019) and

a study on the linkage between high-latitude precipitation and low-frequency variability of the AMOC (Mehling et al. 2023).

The PlaSim-LSG atmosphere includes a wet primitive equation dynamical core governing the conservation of momentum, mass, energy, the specific humidity and the equation of state with hydrostatic approximation (Fraedrich et al. 2005; Lunkeit et al. 2012). The equations are solved on a terrain following σ-coordinate system (pressure divided by surface pressure) with a spectral transform method (Orszag 1970; Eliassen et al. 1970). Parameterizations of unresolved subgrid scale processes include moist and dry convection (Kuo 1965, 1974), clouds (Slingo and Slingo 1991; Stephens et al. 1978, 1984), large-scale precipitation, boundary fluxes of sensible and latent heat and of momentum, long-wave and short-wave radiation (Sasamori 1968; Lacis and Hansen 1974), vertical and horizontal diffusion (Laursen and Eliasen 1989; Louis 1979; Louis et al. 1981) and a land surface scheme with five diffusive layers for temperature and a bucket model for soil hydrology.

The LSG is a three-dimensional global ocean general circulation model based on primitive equations under the assumption of large spatial and temporal scales, using the Boussinesq and hydrostatic approximations and neglecting vertical friction (Maier-Reimer et al. 1993; Maier-Reimer and Mikolajewicz 1992). Turbulent motions are parameterized by a vertical oceanic diffusion coefficient. The LSG model is used to calculate the heat flux from the deep ocean to the mixed-layer due to advective and convective processes, i.e., advection, horizontal diffusion, vertical transport, vertical diffusion, convective adjustments. In contrast, the mixed-layer ocean model is used to compute the temperature tendencies of the mixed-layer due to heat exchanges with the atmosphere.

The thermodynamic sea ice model is based on the zero-layer model of Semtner (1976). This model computes the evolution of the sea ice thickness and surface temperature from the energy balances at the top and bottom of a sea ice-snow layer. The sea ice-snow layer is assumed to have a linear temperature gradient and to have no capacity to store heat. The sea ice concentration is binary, i.e., either a grid cell is fully sea ice covered or open water.

We run the PlaSim-LSG simulations at statistically stationary state with a fixed pre-industrial effective CO_2 volume mixing ratio of 280 ppmv. We perform the runs without diurnal cycle and with seasonal cycle of the solar radiation and each year has 360 days. For the atmosphere, we use a horizontal spectral resolution of T21 (triangular truncation at wavenumber 21 $\sim 5.625° \times 5.625°$ on the corresponding Gaussian grid), ten non-equally spaced sigma-levels up to about 40 hPa in the vertical, a computational time step of 45 min and an output time step of one day. The computational and output time steps of the mixed-layer ocean and

sea ice models are one day. The LSG is run on a 2.5° × 5° staggered E-type grid (Arakawa and Lamb 1977) in the horizontal, with 22 levels in the vertical and with computational and output time steps of 5 days.

2.2 Pan-Arctic sea ice area in the control run

We consider a control run (CTRL) of 3000 years at equilibrium state (Fig. 1; labeled as model years 501-3500; model years 1-500 are discarded as spin-up). From the control run, we derive several experiments with the rare event algorithm (see section 2.3.2). We consider the statistics of the pan-Arctic sea ice area

$$A(t) = \sum_{\phi \geq \phi_{min}} \sum_{\lambda} SIC_{\phi,\lambda}(t) \cdot G_{\phi,\lambda}, \tag{1}$$

where $SIC_{\phi,\lambda}(t)$ is the sea ice concentration at time t in a grid cell centered at latitude ϕ and longitude λ, $G_{\phi,\lambda} = \int_{\phi-\frac{\Delta\phi}{2}}^{\phi+\frac{\Delta\phi}{2}} \int_{\lambda-\frac{\Delta\lambda}{2}}^{\lambda+\frac{\Delta\lambda}{2}} R^2 cos(\phi')d\lambda'd\phi'$ is the grid cell area, R is the earth radius, $\Delta\phi$ and $\Delta\lambda$ are the angular distances between two grid points in the meridional and zonal direction. The summation in (1) includes all ocean grid boxes

north of 40° N (i.e. $\phi_{min} \cdot \frac{180°}{\pi} = 40°$; the black circle in Fig. 1a shows the southern boundary of the domain over which the pan-Arctic sea ice area is computed). The land-sea mask is binary (i.e. a grid cell is either completely ocean or land).

The monthly mean pan-Arctic sea ice area anomalies show interannual variability superimposed on weak fluctuations on multi-year to centennial time scales (Fig. 1b). For example, the sea ice area tends towards positive anomalies between model years 2500 and 2700 and towards negative anomalies around model year 1000 (Fig. 1b). The annual average, the amplitude of the seasonal cycle and the timing of the annual minimum and maximum of the pan-Arctic sea ice area are representative of the observed Arctic sea ice climatology between 1979 and 2015 [cf. Fig. 1a, c and Supplementary Fig. S1a, b; we used data from EUMETSAT Ocean and Sea Ice Satellite Application Facility (2017, 2023) to compare the representation of sea ice in PlaSim-LSG with observations (Supplementary Fig. S1)]. Nevertheless, compared to observations, PlaSim-LSG has a delayed melting period, a positive SIC bias from the Greenland to the Kara Sea and a negative
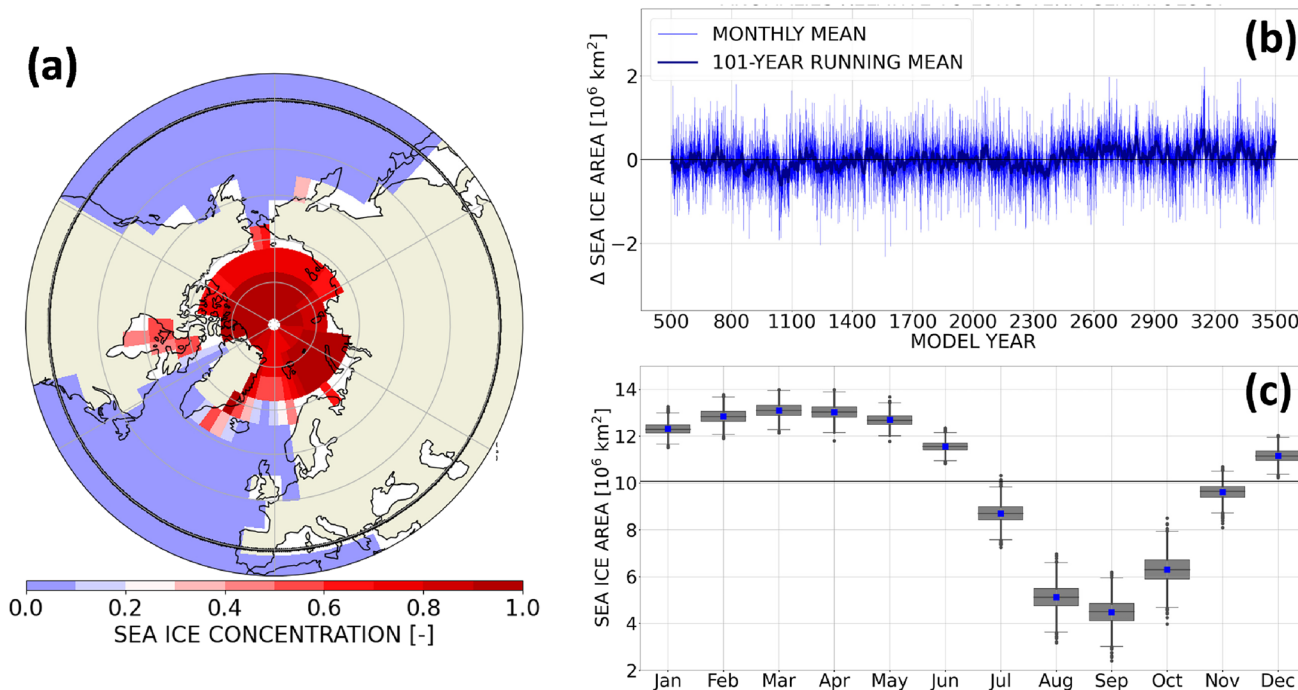

Fig. 1 PlaSim-LSG control run (model years 501-3500): **a** Black circle shows the southern boundary of the domain over which the pan-Arctic sea ice area is computed. Shading shows the climatological annual mean sea ice concentration [–] field. **b** Time series of monthly mean pan-Arctic sea ice area anomalies [10⁶ km²] relative to the climatology of the control run for (blue) the original monthly values and (darkblue) the 101-year running mean. **c** Distributions of monthly mean pan-Arctic sea ice area [10⁶ km²] with respect to the 3000 model years. The averages and medians are given by the blue squares and the horizontal lines in the boxes. The boxes denote interquartile ranges and the maximum whisker length is defined as 1.5 times the interquartile range. The horizontal gray line shows the annual mean pan-Arctic sea ice area

SIC bias western of Greenland (cf. Fig. 1a, c and Supplementary Fig. S1a, b). Despite this, the representation of sea ice dynamics and statistics in PlaSim-LSG is sufficient for the purpose of this study.

We study extreme negative anomalies of February–September (FEBSEP) averaged pan-Arctic sea ice area. We classify a sea ice area anomaly $I'(t)$ as extremely negative if $I'(t) \leq -n\sigma_{CTRL}$, where σ_{CTRL} is the standard deviation of the control run and n is a real-valued number being defined in Sect. 3.

2.3 Rare event algorithm

2.3.1 Description of the method

In climate modeling and weather forecast, ensemble simulations provide a distribution of possible trajectories of the state of the atmosphere or of the climate system. In a conventional ensemble simulation, most of these trajectories correspond to typical fluctuations of an observable, e.g., the pan-Arctic sea ice area. Only a few trajectories lead to extreme states of the observable, which hampers robust statistical and dynamical studies on events that correspond to the tail of the distribution. The genealogical selection algorithm presented in Giardina et al. (2011); Ragone et al. (2018); Ragone and Bouchet (2020, 2021) is designed to guide ensemble simulations to oversample rare dynamical trajectories that lead to extreme anomalies of the time-average of an observable where the averaging time is longer than the typical decorrelation time of the observable. This algorithm is therefore well suited to study the statistics of the seasonally averaged pan-Arctic sea ice area.

We describe the main steps of the algorithm in the following and refer to Ragone et al. (2018) and Ragone and Bouchet (2020, 2021) for more details. We denote $X(t)$ the vector of all model variables at time t. We consider an ensemble of N trajectories $\{X_n(t)\}$ $(n = 1, 2, ..., N)$, an observable $A(\{X_n(t)\})$ (i.e., a function that maps for each trajectory the state vector to a single scalar), a total simulation time T_a and a resampling time τ_r. We start the ensemble simulation from statistically independent initial conditions. We perform at regular times $t_i = i \cdot \tau_r$ $(i = 1, 2, ..., \frac{T_a}{\tau_r})$ a resampling procedure in which trajectories are killed or generate a random number of replicates depending on weights that are related to the magnitude of the time-average of the observable during the past interval. The weights are defined as

$$w_n^i = \frac{e^{k \int_{t_{i-1}}^{t_i} A(\{X_n(t)\}) \, dt}}{R_i} \text{ with } R_i = \frac{1}{N} \sum_{n=1}^{N} e^{k \int_{t_{i-1}}^{t_i} A(\{X_n(t)\}) \, dt},$$
(2)

where R_i is a normalization term and k is a biasing parameter. With a positive (negative) k, the weights favour the replication of trajectories leading to large (small) values of the time-average of the observable during the past interval, while trajectories leading to small (large) values of the time-average of the observable are likely to be killed. The absolute value of k controls the strength of the selection. As described in Ragone et al. (2018), each resampling is performed in such a way that the ensemble size remains constant and equal to N. After the resampling, we slightly perturb the surface pressure field of each trajectory to enable copies of the same trajectory to separate from each other during the subsequent simulation interval (the perturbation is performed as described in the Supporting Information of Ragone et al. (2018)). When the final time T_a is reached, we perform one last resampling and reconstruct an effective ensemble by attaching at each resampling event from the end to the beginning of the simulation the ancestors to the pieces of surviving trajectories. All trajectories that did not survive until the end of the simulation are discarded.

As described in Ragone et al. (2018) and Ragone and Bouchet (2020), one obtains for a large ensemble size N the importance sampling formula

$$\mathbb{P}_k(\{X_n(t)\}_{0 \leq t \leq T_a}) \underset{N \to \infty}{\sim} \frac{e^{k \int_0^{T_a} A(\{X_n(t)\}) \, dt}}{\mathbb{E}_0[e^{k \int_0^{T_a} A(\{X_n(t)\}) \, dt}]} \mathbb{P}_0(\{X_n(t)\}_{0 \leq t \leq T_a}),$$
(3)

where $\mathbb{P}_0$ and $\mathbb{P}_k$ are the probability densities of trajectories in the standard ensemble simulation and in an ensemble generated with the algorithm and $\mathbb{E}_0$ is the expectation value with respect to $\mathbb{P}_0$. The importance sampling formula describes the ratio of probability densities of trajectories in a simulation obtained with the rare event algorithm to the probability density of trajectories according to the real model statistics. Consequently, expectation values (e.g., composites, return times) with respect to the real model statistics can be computed from the data obtained with the rare event algorithm by weighting the contribution of each trajectory to sample averages by the inverse of the exponential factor in (3) (see Ragone et al. 2018; Ragone and Bouchet 2020 Supporting Information of Ragone and Bouchet (2021) for more details).

2.3.2 Set-up of the rare event algorithm experiments

We use as target observable $A(\{X_n(t)\})$ the pan-Arctic sea ice area and perform two sets of experiments with the rare event algorithm. One set is performed with a resampling time of $\tau_r = 30$ days, the other with a resampling time of $\tau_r = 5$ days. Both resampling times are chosen to be smaller than the decorrelation time of the pan-Arctic sea ice area (the autocorrelation function of sea ice area anomalies drops for the first time below 1/e after about 75 days). In this way, the selection favours the survival of trajectories characterized

by large negative time-persistent sea ice area anomalies during the interval prior to a resampling event. In contrast to the resampling time of $\tau_r = 30$ days, the resampling time of $\tau_r = 5$ days is not larger than the persistence time scale of the large-scale atmospheric circulation (Baldwin et al. 2003) and is only slightly larger than the typical persistence of synoptic-scale atmospheric fluctuations (Hoven 1957). We therefore expect that the experiments with a resampling time of $\tau_r = 5$ days efficiently sample extremely low sea ice states both due to anomalies in the oceanic thermal state and due to anomalies in the atmospheric circulation that are in the order of or larger than the upper range of the synoptic time scale. In contrast, the experiments with a resampling time of $\tau_r = 30$ days are primarily designed to increase the sampling efficiency of oceanic drivers of low sea ice states. In this case, we expect atmospheric drivers of sea ice reduction to be sampled only if they are characterized by an anomalously large persistence (e.g., an one month long persistent negative phase of the summer AO).

Both sets of experiments include $M = 5$ ensemble simulations labelled with $m = 1, ..., M$ (Table 1). Each ensemble has $N = 600$ trajectories and a total simulation time of $T_a = 240$ days between February 1st and September 30th. We take different values of the biasing parameter for the different experiments: $k = -0.06 \cdot 10^{-6}$ km^{-2} day^{-1} for ensemble $m = 1$, $k = -0.05 \cdot 10^{-6}$ km^{-2} day^{-1} for ensembles $m = 2$ and $m = 4$ and $k = -0.04 \cdot 10^{-6}$ km^{-2} day^{-1} for ensembles $m = 3$ and $m = 5$. While the precise values of k is chosen empirically, a reasonable order of magnitude of the parameter can be derived using a scaling argument presented in Ragone and Bouchet (2020) and in the Supporting Information of Ragone and Bouchet (2021). According to this scaling argument, the selected k-values correspond to a shift of the peak of the distribution of February-September mean pan-Arctic sea ice area anomalies to values between $-0.5 \cdot 10^6$ km^2 and $-0.75 \cdot 10^6$ km^2, which corresponds to a range of estimated return times between 100 and 1000 years (see Sect. 3.1).

Table 1 600-member rare event algorithm ensemble simulations running between February 1st and September 30th

m	Model years for initial condition	Biasing parameter k [10^{-6} km^{-2} day^{-1}]
1	501, 506,..., 3496	-0.06
2	502, 507,..., 3497	-0.05
3	503, 508,..., 3498	-0.04
4	504, 509,..., 3499	-0.05
5	505, 510,..., 3500	-0.04

This set-up applies both to the experiments with a resampling time of $\tau_r = 5$ days and to the experiments with a resampling time of $\tau_r = 30$ days

For each ensemble, the inital condition for trajectory $n = 1, ..., N$ is taken from February 1st in year $500 + m + 5(n - 1)$ of the control run (Table 1). In order to have a baseline for the statistics, we also subdivide the 3000-year control run into five 600-member control ensembles such that the rare event algorithm ensemble m has exactly the same initial conditions as the control ensemble m. Sampling the initial conditions with a gap of 5 years ensures that sea ice area anomalies in the different trajectories within an ensemble are approximately independent from each other.

3 Results

3.1 Importance sampling of summer seasons with extremely low pan-Arctic sea ice area

Our goal of using the rare event algorithm is to improve the sampling efficiency of extreme negative pan-Arctic sea ice area anomalies on average over the extended summer season between February and September. We show the seasonal evolution of daily pan-Arctic sea ice area anomalies merged over the two rare event algorithm experiments with $k = -0.05 \cdot 10^{-6}$ km^{-2} day^{-1} (Fig. 2a, b). Throughout the season, trajectories generated with the rare event algorithm show a systematic shift towards lower sea ice area values compared to the control run. The amplitude of this shift does not differ between the 5-days and the 30-days resampling time experiments and is more than twice as large after July than between February and June. The amplification of the shift during July coincides with an increase in the climatological sea ice area variability of the control run (cf. Figs. 1c and 2a, b).

The systematic biasing towards negative sea ice area anomalies both in the 5-days and 30-days resampling time experiments emerges from the trajectory resampling at intervals shorter than the decorrelation time of the sea ice area. During each resampling event, trajectories characterized by large negative time-persistent sea ice area anomalies form replicas at the expense of trajectories with less negative sea ice area anomalies. After the simulation, the surviving pieces of trajectories are reconstructed into an effective ensemble. As a consequence, the rare event algorithm efficiently performs importance sampling of trajectories that lead to extreme negative February–September time-averaged sea ice area anomalies (Fig. 2). The control distribution of February–September mean sea ice area anomalies has a standard deviation of about $0.25 \cdot 10^6$ km^2 and a minimum value of $-0.80 \cdot 10^6$ km^2. In contrast, the sea ice area anomalies obtained with the rare event algorithm fluctuate around a mean value of $-0.6 \cdot 10^6$ km^2 and have minima at $-0.89 \cdot 10^6$ km^2 (30-days resampling time experiments) and at $-0.99 \cdot 10^6$ km^2 (5-days
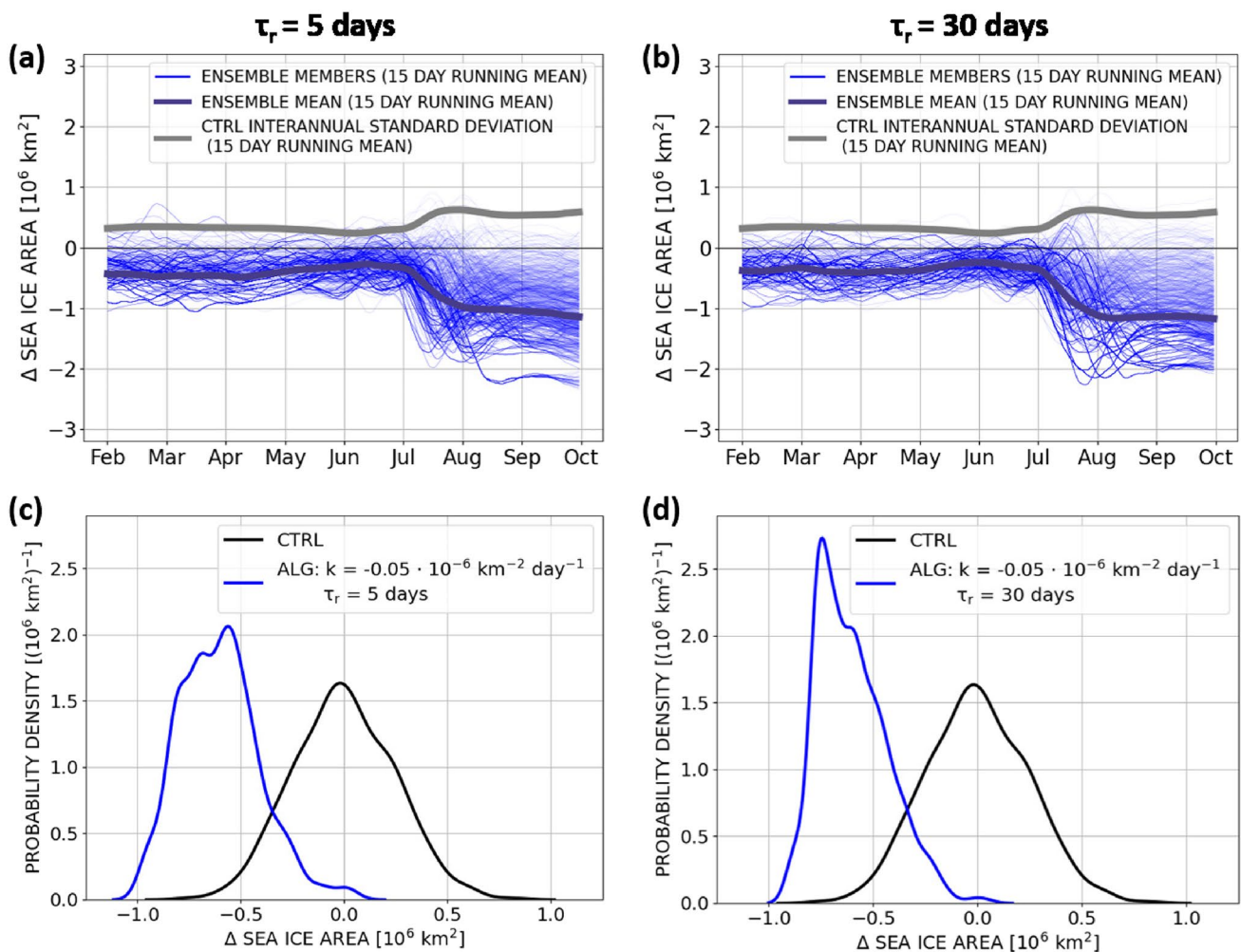
Fig. 2 a, b Trajectories (thin blue lines) and ensemble mean (thick blue line) of daily pan-Arctic sea ice area anomalies in rare event algorithm ensemble simulations two and four, i.e. with $k = -0.05 \cdot 10^{-6}$ km^{-2} day^{-1}, for **a** a resampling time of 5 days and **b** a resampling time of 30 days. The anomalies are evaluated relative to the daily climatology of the control ensembles two and four. Only the trajectories that survived until the final simulation time are plotted and are used for the computation of the ensemble mean. The gray lines show the climatological standard deviation of daily sea ice area anomalies in resampling time experiments. The simulations with the the control ensembles m = 2 and m = 4. **c, d** Probability distribution functions of February–September mean pan-Arctic sea ice area anomalies relative to the control climatology for **c** a resampling time of 5 days and **d** a resampling time of 30 days. (Black) Anomalies of the control run itself merged over ensembles m = 2 and m = 4 and (blue) anomalies in the rare event algorithm experiments corresponding to ensembles m = 2 and m = 4, i.e. with $k = -0.05 \cdot 10^{-6}$ km^{-2} day^{-1} (exclusively based on the trajectories that survived until the end of the simulation)

resampling time experiments). The simulations with the rare event algorithm require the same computational cost as the control run, but strongly populate the lower tail of the distribution of FEBSEP mean pan-Arctic sea ice area anomalies (Fig. 2c, d; we refer to the Supplementary Information S2 and Supplementary Figs. S5 and S6 for more details about the adequacy of the rare event simulations used in this work, i.e., of the extent to which the effective ensembles contain sufficiently enough different initial-time ancestors with a non-zero number of final-time decendants to gather robust statistics).

Return times are an important characterization of extreme events. They indicate the average waiting time between

events of size larger than a given amplitude. We compare return times of FEBSEP mean pan-Arctic sea ice area anomalies between the control run and the experiments with the rare event algorithm (Fig. 3a, b). For the computation of the return times, we proceed similarly to the modified block maximum estimator presented in Lestang et al. (2018) and in the Supporting Information of Ragone et al. (2018). Accordingly, an estimate of the return time is given by

$$r(a) = -\frac{\Delta T}{\ln[1 - \frac{1}{N}\sum_{n=1}^{N} \mathbb{1}_a(I_n)]} \quad \text{with} \quad \mathbb{1}_a(I_n) = \begin{cases} 1, & I_n \leq a, \\ 0, & I_n > a, \end{cases}$$
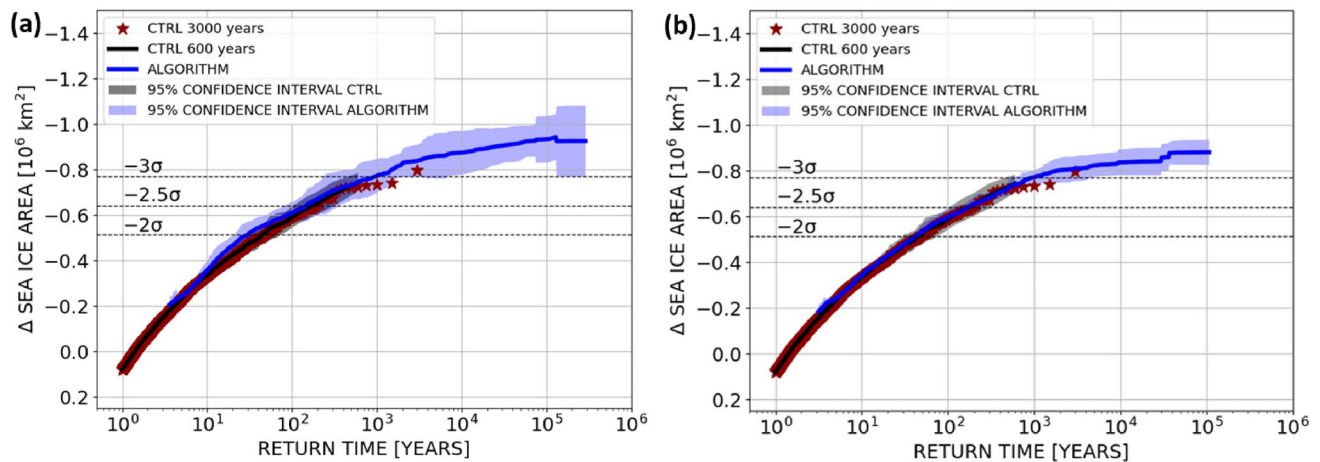
(4)

Fig. 3 Return curves for February–September mean pan-Arctic sea ice area anomalies relative to the control run. (Red stars) The direct estimate of return times from the 3000 year control run, (black line) the average estimate over the five 600-member ensembles of the control run and (blue line) the average estimate over the overlap of at least three out of five 600-member rare event algorithm experiments. Shading denotes the 95% confidence interval obtained from the statistics of the three to five estimates assuming a Student's *t* distributed estimator (see Supplementary Information S1). **a** Rare event algorithm with 5-days resampling time and **b** with 30-days resampling time. The dashed lines in **a** and **b** indicate anomalies of minus two, minus two and a half and minus three standard deviations with respect to the control run

where I_n is the February-September time-averaged pan-Arctic sea ice area anomaly in trajectory n, a is the return level of a sea ice area anomaly, N the number of trajectories, ΔT is the block length of one year and $\mathbb{1}_a(I_n)$ is the indicator function. As described in Lestang et al. (2018) and in the Supporting Information of Ragone et al. (2018), Eq. 3 can be used to compute the return times from the simulations with the rare event algorithm. Note that for large values of the return time, the formula in (4) is approximately equivalent to $r(a) = T_d / \sum_{n=1}^N \mathbb{1}_a(I_n)$, where $T_d = N\Delta T$ is the total length of the time series (see Lestang et al. (2018)).

In Fig. 3, the red curves show return time estimates obtained from the 3000-year control run. In order to estimate uncertainty ranges, we subdivide the control run into five 600-member ensembles (see Sect. 2.3.2) providing five return time estimates. We compute the average over these five estimates (black curve) and use their empirical standard deviation to construct 95% confidence intervals (black shading; see Supplementary Information S1 for more details). In the same way, the blue lines and blue shading show the average return time estimates and confidence intervals obtained from the overlapping output of at least three out of the five 600-member rare event algorithm experiments (note that rare event algorithm experiments with slightly different k values cover slightly different ranges of sea ice area anomalies). Both for the 5-days and for the 30-days resampling time experiments, the return curves for the control run and for the rare event algorithm overlap in a range of sea ice area anomaly values. This range corresponds to an overlap between the probability distribution functions of sea

ice area anomalies obtained with the control and rare event algorithm ensembles (cf. Figs. 2c, 3a, Supplementary Fig. S2a, c and Figs. 2d, 3b, Supplementary Fig. S2b, d). Consequently, the rare event algorithm consistently computes the probabilities that trajectories generated with the algorithm have with respect to the real model statistics (an analysis of the differences between the control and rare event algorithm estimates of the return levels shows that both estimates are statistically consistent with each other at least for a return time range between a couple of decades and about 750 years (Supplementary Fig. S3a, b)).

The major advantage of computing the return times with the rare event algorithm compared to the control run is the access to much rarer events with the former than with the latter. From the control run, we cannot accurately estimate return times of more than 1000 years. The rare event algorithm experiments are conducted with the same computational cost as the control run (i. e. 3000 years), but allow to compute return times up to 10^5 years with uncertainty ranges comparable with the control run ones for return times of several hundreds of years. Hence the algorithm increases the sampling efficiency of extreme negative February–September mean sea ice area anomalies by two to three orders of magnitude. The plateaux at return times larger than 10^5 years (Fig. 4a) and larger than $5 \cdot 10^4$ years (Fig. 4b) are due to undersampling as discussed in Lestang et al. (2018) and in the Supporting Information of Ragone et al. (2018).

The result has the following implications. Firstly, the rare event algorithm provides access to ultra-rare sea ice area anomalies that do not occur in the control run. An unrealistic
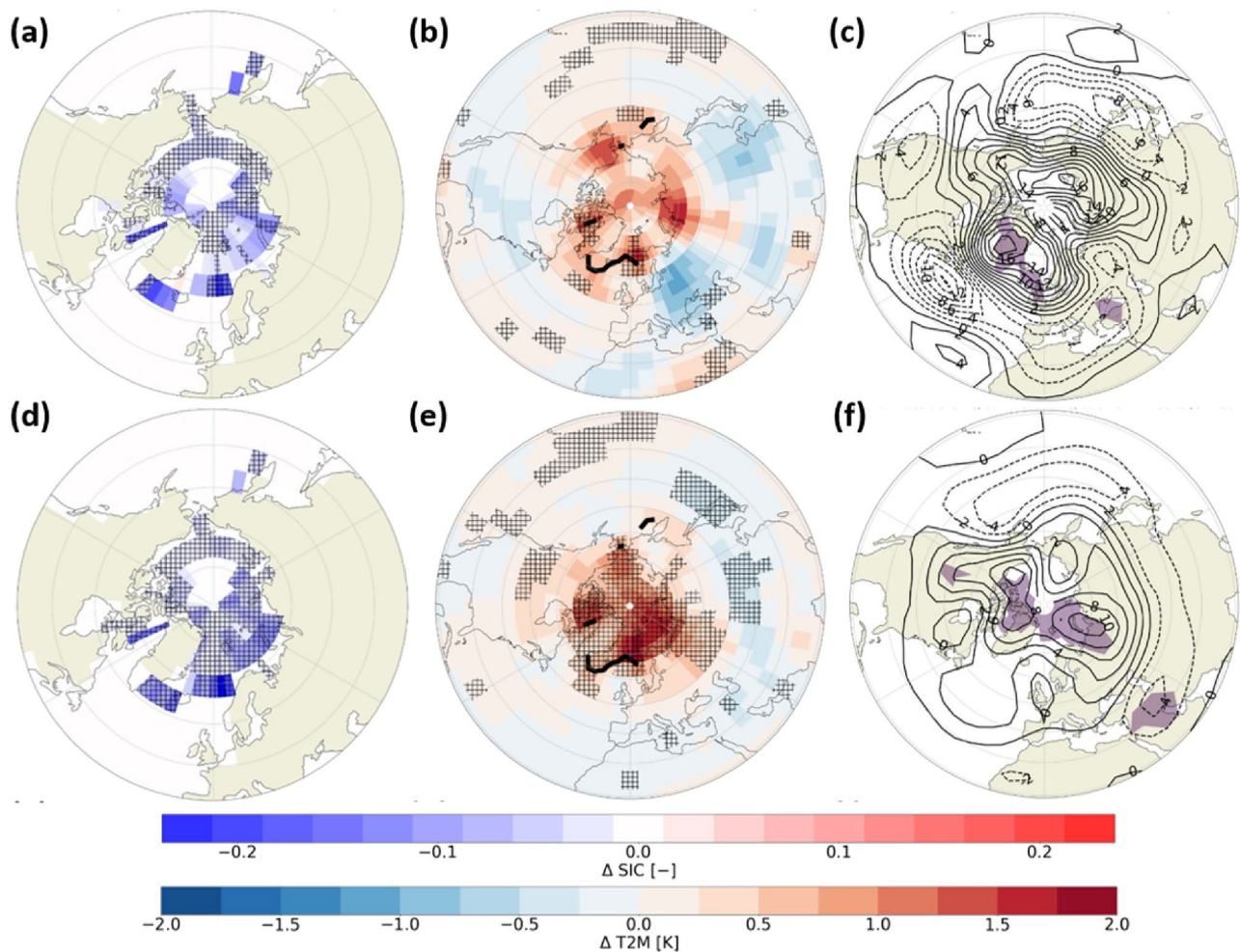
Fig. 4 Composite mean February-September averaged **a**, **d** sea ice concentration (SIC [-]), **b**, **e** two metre temperature (T2M [K]) and **c**, **f** 500 hPa geopotential height (Z500 [gpm]; contour interval two gpm) anomalies conditional on extreme negative February–September mean pan-Arctic sea ice area anomalies equal or smaller than − 2.5 standard deviations of the control ensembles (corresponds to extremes with return times of more than 200 years). Composite maps are presented as an average over **a–c** the five control and **d–f** the five rare event algorithm experiments with a resampling time of $\tau_r = 5$ days. All anomalies are estimated with respect to the climatology of the control ensembles. The hatching in (**a**, **b**, **d**, **e**) and shading in (**c**, **f**) denote statistical significance at the 5% level according to a two-sided t test (see the Supplementary Information S1 for more details). The black contour line in (**b**, **e**) indicates the climatological February–September mean sea ice edge defined as the 15% sea ice concentration line

amount of computational cost would be required to observe them with direct sampling. Secondly, the algorithm enriches the general statistics of the extremes. While the control run delivers only a few events with a sea ice area anomaly in the order of three standard deviations away from the climatology, hundreds of them are available in the experiments with the algorithm. Thirdly, the return curve obtained with the 5-days resampling time experiments extends only to marginally larger amplitudes of sea ice area anomaly values than the one obtained with the 30-days resampling time experiments. Thus, the targeted sampling of drivers of sea ice reduction acting on the upper range of synoptic and on submonthly time scales only marginally increases the magnitude of the most extreme negative February–September

mean pan-Arctic sea ice area anomalies. We will further address this point in section 4.

3.2 Sea ice conditions and state of the atmosphere during summer seasons of extremely low sea ice area

We perform composite analyses to investigate and characterize the average states of the sea ice and of the atmosphere during summer seasons of extreme negative February–September mean pan-Arctic sea ice area anomalies. Composites mathematically correspond to conditional expectation values that we estimate as

$$\mathbb{E}_0[O(\{X_n(t)\}) \mid I_n \le -m\sigma] = \frac{\mathbb{E}_0[O(\{X_n(t)\}) \cdot \mathbb{1}(-I_n - m\sigma)]}{\mathbb{E}_0[\mathbb{1}(-I_n - m\sigma)]},$$
$$(5)$$

where $O(\{X_n(t)\})$ and I_n are the anomalies of a target climate variable (e.g., 500 hPa geopotential height) and of the February–September mean pan-Arctic sea ice area in trajectory n, σ is the control run standard deviation of I, m a positive integer and $\mathbb{1}(-I_n - m\sigma)$ is the indicator function with

$$\mathbb{1}(-I_n - m\sigma) = \begin{cases} 1, & -I_n - m\sigma \ge 0 \\ 0, & -I_n - m\sigma < 0 \end{cases}. \qquad (6)$$

All anomalies are evaluated relative to the climatology of the control ensembles and $\mathbb{E}_0$ is the expectation operator with respect to the unbiased model statistics (i.e. the statistics of the control run). By using Eq. 3, composites can be computed from the output of the rare event algorithm as described in Ragone and Bouchet (2020) and in the Supporting Information of Ragone et al. (2018) and of Ragone and Bouchet (2021).

One advantage of the rare event algorithm is that it provides more accurate composite estimates for large return times than the control run. For the subsequent analyses, we compute composite estimates for each of the five rare event algorithm ensembles and consider the average over the five estimates respectively. We assess the statistical significance of the composite maps by applying a two-sided t-test to the set of the five estimates (see Supplementary Information S1). We apply the same procedure to five 600-member control ensembles obtained from the 3000-year control run (see Sect. 2.3.2). All subsequent results obtained with the rare event algorithm are based on the experiments with a resampling time of $\tau_r = 5$ days. As explained in Sect. 2.3.2, this value of resampling time allows to increase the sampling efficiency of a broader range of physical processes compared to a resampling time of $\tau_r = 30$ days.

3.2.1 Seasonal mean states of the sea ice and of the atmosphere

We compare the control run and rare event algorithm estimates of average seasonal mean SIC, two metre temperature (T2M) and 500 hPa geopotential height (Z500) anomalies during summer seasons of extreme negative pan-Arctic sea ice area anomalies with return times of more than 200 years (i.e. $I_n \le -2.5\sigma$) (Fig. 4). For this threshold, we have access to several hundreds of events with the algorithm and to 13 events with the control run. While the algorithm and control estimates consistently indicate a warm Arctic state during extremely low sea ice seasons, the benefit of the algorithm manifests in the larger statistical accuracy of the estimates compared to the control run. The algorithm composites indicate statistically significant negative mean SIC anomalies

in the North Atlantic side of the Arctic, along the Russian coast and in the marginal seas of the Pacific side of the Arctic Ocean (Fig. 4d). Statistically significant positive T2M anomalies occur over the entire Arctic Ocean with largest amplitudes over the Canadian Archipelago, Greenland and Kara Seas (Fig. 4e). The anomalously warm surface conditions are accompanied by positive Z500 anomalies over the Arctic reaching statistical significance from the Canadian Archipelago over Svalbard to the Barents and Kara Seas. Compared to the algorithm, the control run estimates of the mean SIC, T2M and Z500 anomalies are statistically significant in a much smaller amount of grid cells. Apart from the formal statistical significance, the larger amount of extreme events available through the algorithm decreases the likelihood that the composite maps include noisy patterns that are not statistically related to the sea ice area anomalies and that are occurring in the control run by the effect of sampling (Fig. 4b, c, e, f).

3.2.2 Seasonal evolution of the states of the sea ice and of the atmosphere

We are interested in the physical processes favouring anomalously warm Arctic states with extremely low pan-Arctic sea ice area during summer. From the physical point of view, understanding the drivers of extremely low pan-Arctic sea ice area is hindered by at least two factors. Firstly, a variety of feedback mechanisms occur in the Arctic climate system (e.g., Screen and Simmonds 2010; Serreze and Francis 2006) and can lead to ambiguities of cause and effect relationships between different quantities. This applies, for example, to the relationship between the anomalously warm Arctic atmosphere and the negative sea ice concentration anomalies shown in Fig. 4. The negative sea ice concentration anomalies are potentially driven by the anomalous warm atmosphere. At the same time, however, the positive T2M and Z500 anomalies are potentially a consequence of the anomalous heat flux from the ocean to the atmosphere that results from the reduced sea ice cover. Secondly, extremely low summer pan-Arctic sea ice area may be generated in two different ways. Are we sampling trajectories in which processes on intra-seasonal time scales lead to an extreme reduction of the pan-Arctic sea ice area within a season? Or are we sampling trajectories in which extreme negative February–September mean pan-Arctic sea ice area anomalies are related to preconditioning (cf. Chevallier and Salas-Mélia 2012; Holland et al. 2011; Kauker et al. 2009)?

We firstly identify to what extent extreme negative February–September mean pan-Arctic sea ice area anomalies are related to intra-seasonal sea ice reduction vs. pre-existing anomalies in the sea ice state originating from the previous winter. For this purpose, we analyse the seasonal evolution of mean pan-Arctic sea ice area and sea ice volume

anomalies conditional on the occurrence of summer seasons of extremely low pan-Arctic sea ice area (Fig. 5). On average, extreme negative FEBSEP pan-Arctic sea ice area anomalies are related both to persistent sea ice area anomalies originating from the previous winter and to anomalous sea ice area reduction between late spring and late summer (Fig. 5a). The sea ice area anomalies between February–March and May–June are in the order of one and two-thirds of the interannual standard deviation and have an approximately constant level of about $-0.2 \cdot 10^6$ km^2 to $-0.5 \cdot 10^6$ km^2. In contrast, the sea ice area anomalies in August–September are in the order of $-1 \cdot 10^6$ km^2 to $-1.5 \cdot 10^6$ km^2, two to three times as large in magnitude as the interannual standard deviation. As a consequence, the anomalies in the sea ice area reduction between February–March and August–September are about twice as large in magnitude as the pre-existing sea ice area anomalies in late winter. The relative importance of intra-seasonal sea ice area reduction over pre-existing sea ice area anomalies slightly increases with the amplitude of the extremes of the February–September mean pan-Arctic sea ice area anomalies (Fig. 5a).

In contrast to the pan-Arctic sea ice area, pan-Arctic sea ice volume anomalies are directly related to the amount of energy required to produce these anomalies and their seasonal evolution does not directly depend on the open-water-formation-efficiency given by the sea ice thickness field. Pre-existing pan-Arctic sea ice volume anomalies originating from the previous winter are three to four times as large as the anomalies in their reduction from February–March to August–September (Fig. 5b). This result points at a strong contribution of preconditioning of extreme anomalies of the

FEBSEP mean pan-Arctic sea ice area through an extremely low winter pan-Arctic sea ice volume, which is both due to negative anomalies in the winter pan-Arctic sea ice area and in the winter pan-Arctic mean sea ice thickness field (cf. Fig. 5 and Supplementary Fig. S4a, b). On top of the preconditioning, an anomalous intra-seasonal reduction in the sea ice volume occurs between April–May and July–August. This suggests a contribution of intra-seasonal dynamics to extreme negative FEBSEP sea ice area anomalies in addition to the preconditioning.

We analyse the seasonal evolution of T2M and Z500 anomalies conditional on extremely low sea ice summer seasons to establish a link between the sea ice lows and the thermodynamic and dynamic states of the atmosphere (Fig. 6). During extremely low sea ice summers, positive temperature anomalies pre-exist over the Arctic during the beginning of the simulation period in February–March, especially from the Greenland to the Kara Seas and over the Canadian Archipelago (Fig. 6a). Positive T2M anomalies over the Arctic Ocean persist until spring before they largely disappear in June-July (Fig. 6a–d). A reemergence of significant positive two metre temperatures occurs in August–September over the Arctic Ocean, though with a much smaller amplitude than at the beginning of the season (Fig. 6a, e). Possible causes for the anomalously warm atmosphere in late winter and spring include enhanced poleward atmospheric heat and moisture transport (e.g., Alekseev et al. 2019), enhanced poleward oceanic heat transport (e.g., Swaluw et al. 2007; Jungclaus and Koenigk 2010), an anomalously strong conductive heat flux within an anomalously thin sea ice (see Semtner (1976) for a description of the thermodynamics of sea ice) and enhanced open water area related to negative
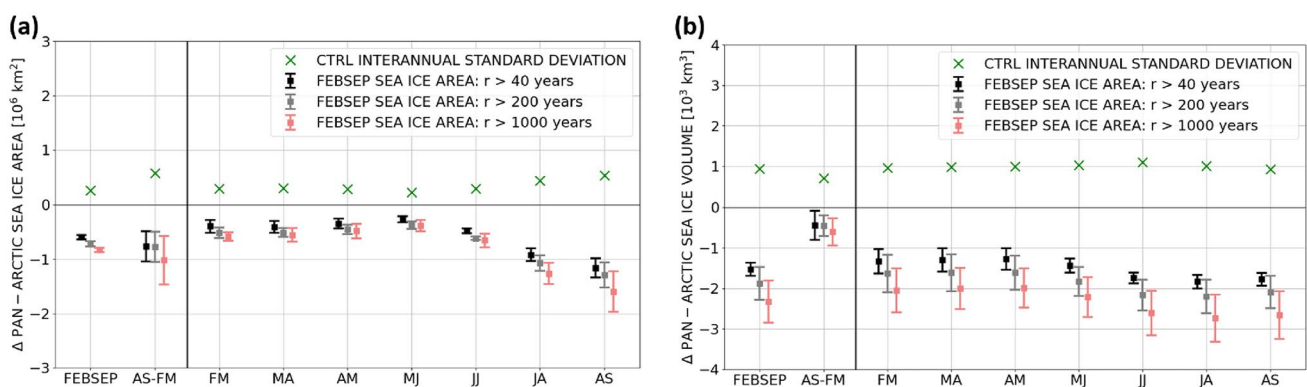

Fig. 5 Rare event algorithm experiments with a resampling time of $\tau_r = 5$ days: Composite mean **a** pan-Arctic sea ice area anomalies [10^6 km^2] and **b** pan-Arctic sea ice volume anomalies [10^3 km^3] conditional on extreme negative February–September mean pan-Arctic sea ice area anomalies equal or smaller than (black) -2 standard deviations, (gray) -2.5 standard deviations and (red) -3 standard deviations of the control ensembles (roughly corresponds to extremes with return times of more than 40, 200 and 1000 years). The anomalies are

computed with respect to the control climatologies of the five control ensembles. The composite estimates are presented as an average over the five rare event algorithm ensembles and the error bars represent 95% confidence intervals (see Supplementary Information S1). "AS-FM" denotes the difference between August–September (AS) and February–March (FM) and the green "x" markers indicate the climatological standard deviation in the control run
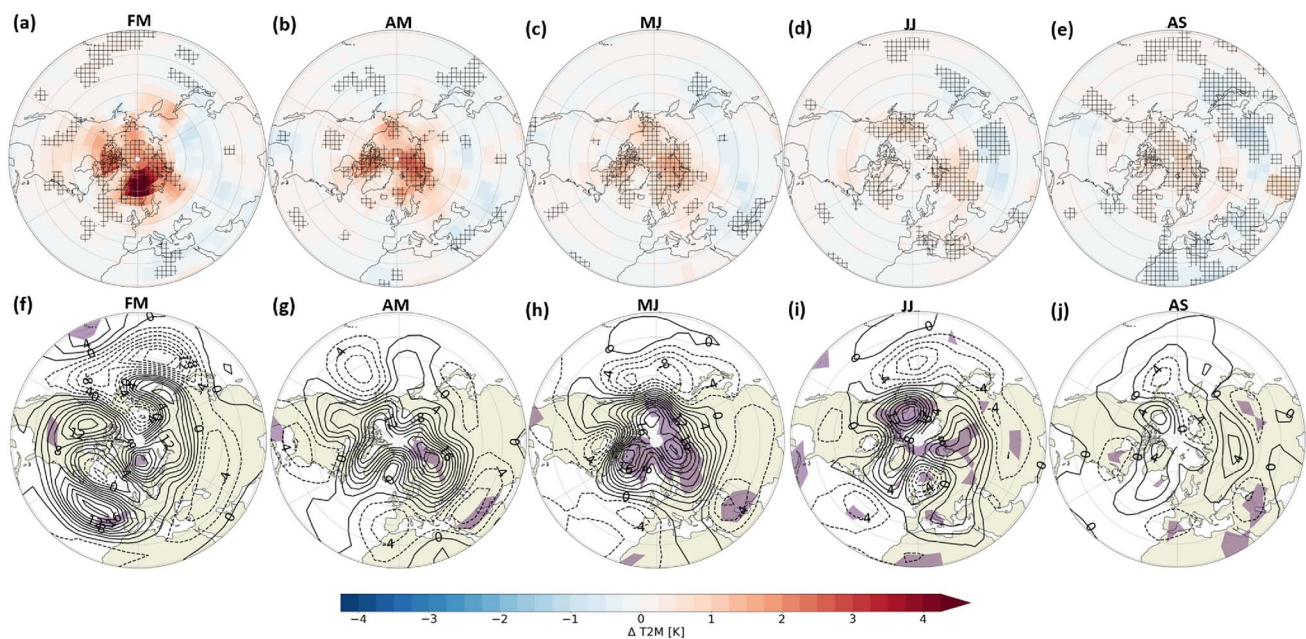
Fig. 6 Composite mean **a–e** two metre temperature (T2M [K]) and **f–j** 500 hPa geopotential height (Z500 [gpm]; contour interval two gpm) anomalies conditional on extreme negative February–September mean pan-Arctic sea ice area anomalies presented as an average over the five rare event algorithm ensembles. The T2M and Z500 anomalies are averaged over **a, f** February–March (FM), **b, g** April–May (AM), **c, h** May–June (MJ), **d, i** June–July (JJ), **e, j** August–September (AS) and are respectively estimated relative to the climatology of the control ensembles. The sea ice area anomalies are classified as "extreme" if the sea ice area anomaly is smaller than −2.5 standard deviations of the control ensembles. The hatching in **a–e** and the shading in **f–j** denote statistical significance at the 5% level according to a two-sided t test

sea ice area anomalies (Screen and Simmonds 2010). Since the positive T2M anomalies in late winter and spring coincide with negative sea ice area and thickness anomalies (cf. Figs. 5a, 6a–c and Supplementary Fig. S4), we expect that an increased upward surface sensible heat flux both due to enhanced upward conductive heat flux within an anomalously thin sea ice and due to reduced sea ice area contributes to the positive T2M signal. The decline of the magnitude of the T2M anomalies in summer is consistent with a constraint due to the climatological sea ice melting. Near-surface temperatures are at the freezing point and any additional heat input would accelerate sea ice melt, but not warm the air. The weak positive T2M signal in August–September could both be a consequence of an anomalously large amount of open water and a driver of sea ice reduction.

Positive geopotential height anomalies pre-exist over the Arctic at the beginning of the simulation period, even though they are statistically significant only in a few grid points (Fig. 6f, g). From April–May to May–June, they become instead statistically significant over large part of the Arctic (Fig. 6g, h), while the positive T2M anomaly signal at the surface is decreasing (Fig. 6b, c). This suggests that anomalies in the atmospheric circulation in late spring and summer are not a pure consequence of the diabatic heating from the anomalously warm surface, but that on the contrary in this period it is the atmospheric dynamics that plays an active role in contributing to the reduction of sea ice.

3.3 Surface energy budget and feedback mechanisms

We perform a surface energy budget analysis for two purposes. Firstly, we are interested in the amount of anomalous energy accumulation in the snow-sea ice-ocean system that is related to surface-atmosphere energy flux anomalies between February and September. Secondly, we exploit the impact of the thermodynamic atmospheric state (e.g., temperature, water vapour, clouds) on the surface energy fluxes to understand how extreme negative pan-Arctic sea ice area anomalies are physically related to anomalous atmospheric conditions. We define the surface energy budget for an infinitesimally thin interface without heat storage located between the atmosphere and the snow-sea ice-ocean system (cf. Serreze and Barry (2014)). The different terms of the budget are then given by

$$R_{SW}(1 - \alpha) + R_{LW} + S + L = -\epsilon \sigma T_s^4 + Q + M, \tag{7}$$

where R_{SW} and R_{LW} are the downward shortwave and downward longwave radiative fluxes, respectively; α is the surface albedo, S and L are the sensible and latent heat fluxes, ϵ

is the surface emissivity, $\sigma = 5.67 \cdot 10^{-8}$ W m^{-2} K^{-4} is the Stefan–Boltzmann constant and T_s is the surface temperature. Q summarizes conductive and turbulent energy fluxes between the surface and the snow-sea ice-ocean system. M is the energy exchange associated with melting and freezing at the surface. Energy fluxes related to bottom sea ice growth, to temperature changes in the snow-sea ice-ocean system and the vertical energy flux from the ocean into the sea ice are implicitly included in Q. If not stated otherwise, we define upward (downward) energy fluxes and associated flux anomalies to be positive (negative).

During summer seasons of extremely low pan-Arctic sea ice area, negative net surface-atmosphere energy flux anomalies occur over the Arctic Ocean and correspond to an anomalous energy accumulation within the snow-sea ice-ocean system (Fig. 7a). The domain-average of these

anomalies over all ocean grid boxes north of 70° N is − 2.14 Wm^{-2}, which corresponds to a domain- and season- (February–September) integrated net energy accumulation of about $4.5 \cdot 10^{20}$ J. This amount of energy would be sufficient to melt about $1.48 \cdot 10^{3}$ km^{3} of sea ice, which is about three quarters of the February–September mean pan-Arctic sea ice volume anomaly being present during summer seasons of extremely low pan-Arctic sea ice area (Fig. 5b). A direct contribution of the net accumulation of energy to the anomalies in the sea ice volume is, however, difficult for following reasons. One part of the energy is used to increase the temperature of the snow-sea ice-ocean system instead of being used for melting and an important part of the sea ice volume anomaly is already existing in late winter (Fig. 5b). Likewise, the domain-average north of 70° N is limited to representing the vertical surface
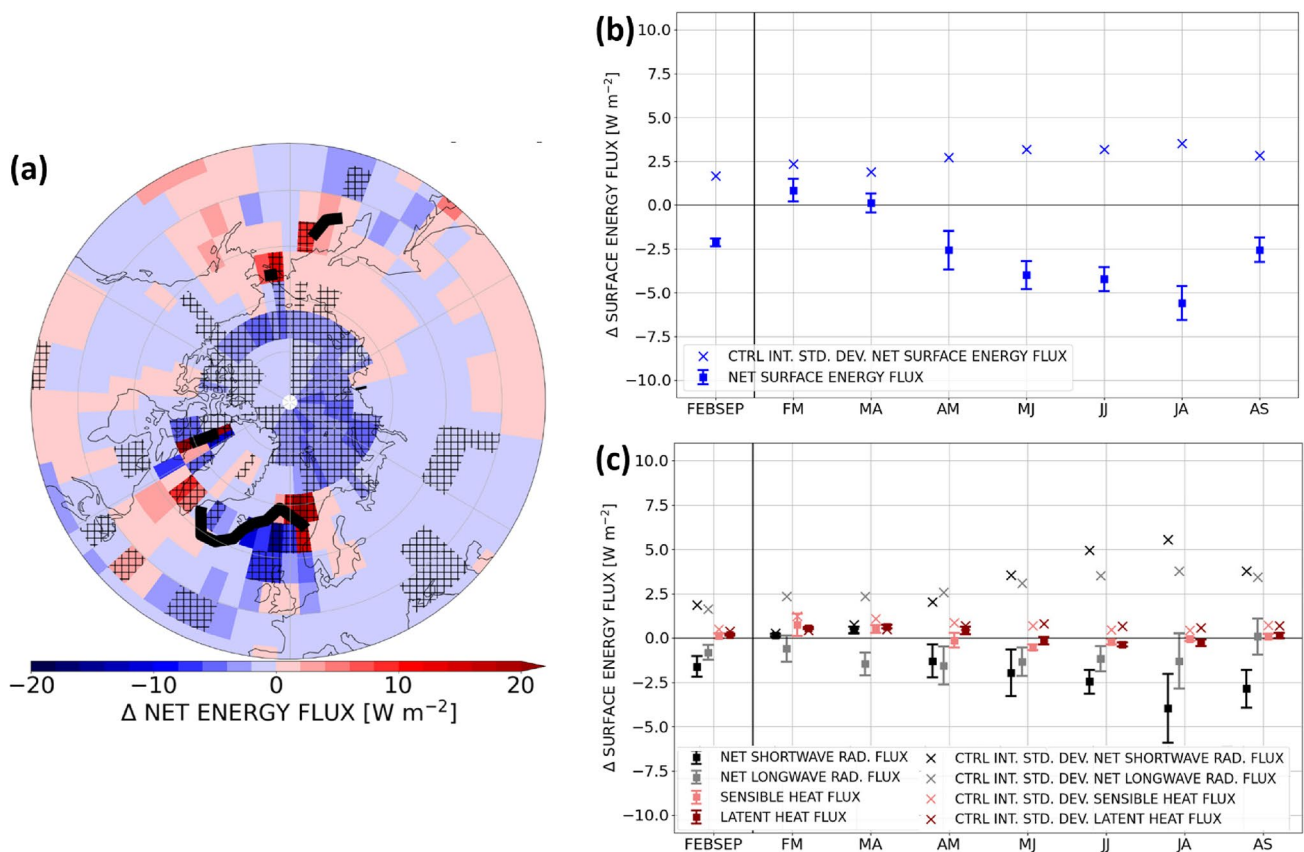
Fig. 7 Rare event algorithm experiments with a resampling time of $\tau_r = 5$ days: Composite mean surface energy flux [Wm^{-2}] anomalies conditional on extreme negative February–September mean pan-Arctic sea ice area anomalies equal or smaller than −2.5 standard deviations of the control ensembles. Mean anomalies are presented as an average over the five rare event algorithm experiments and are evaluated relative to the control run. Hatching in **a** indicates statistical significance at the 5% level and error bars in **b–c** show 95% confidence intervals obtained from the statistics of the five estimates (see Supplementary Information S1). **a** February–September mean net surface-

atmosphere energy flux anomalies (sensible + latent + net longwave + net shortwave). February–September and bimonthly mean domain-averaged **b** net surface-atmosphere energy flux anomalies and **c** surface sensible and latent heat flux and net shortwave and net longwave radiative flux anomalies. The averaging is performed over all ocean grid boxes north of 70° N. The "x" markers respectively indicate the climatological standard deviations in the control run. The black contour line in **a** indicates the climatological February–September mean sea ice edge defined as the 15% sea ice concentration line

energy flux anomalies in the high Arctic, while the sea ice extends much further to the south during winter and spring. Nevertheless, the result indicates that the net February–September mean energy exchange between the atmosphere and the Arctic Ocean surface provides a substantial amount of energy potentially available to contribute to enhanced intra-seasonal sea ice reduction.

We are interested in the physical processes that drive the anomalous net energy transfer from the atmosphere to the Arctic Ocean during extremely low sea ice summers. For this purpose, we investigate how the net atmosphere-surface energy flux anomalies are partitioned into their different components over the course of the season (Fig. 7b, c). Both the net atmosphere-surface energy flux anomalies and their different components exhibit a pronounced seasonality. An enhanced net energy transfer from the atmosphere to the snow-sea ice-ocean system occurs between April–May and August–September, which includes the period of anomalous intra-seasonal reduction in the pan-Arctic sea ice area and sea ice volume (cf. Figs. 5 and 7b). In contrast, slightly positive net atmosphere-surface energy flux anomalies indicate a small anomalous release of energy from the Arctic Ocean to the atmosphere in late winter (Fig. 7b). The latter is consistent with a contribution of preconditioning via the winter sea ice-ocean state to extremely low FEBSEP pan-Arctic sea ice area (see Sect. 3.2.2).

Regarding the entire season, the net atmosphere-surface energy flux anomalies are dominated by the radiative (net shortwave and net longwave radiation) compared to the non-radiative (sensible and latent heat) fluxes (Fig. 7c). Slightly positive non-radiative flux anomalies explain the small anomalous energy transfer from the Arctic Ocean to the atmosphere in late winter, while negative sensible heat flux anomalies in May–June suggest a direct contribution of anomalously high air temperatures to enhanced snow-sea ice-ocean warming or to enhanced snow-sea ice melt. The negative sensible heat flux anomalies in May–June coincide with the appearance of a statistically significant positive Z500 anomaly pattern and thus with an anomalously warm state of the lower troposphere (cf. Figs. 6 and 7c). A strong contribution of net shortwave radiative fluxes to the seasonal accumulation of energy in the Arctic Ocean occurs between April–May and August–September. The net longwave radiative flux anomalies are smaller in magnitude than the shortwave ones, but still contribute to a statistically significant anomalous accumulation of energy in the Arctic Ocean between March–April and June–July. An enhanced net longwave radiative forcing on the Arctic sea ice during spring is consistent with Kapsch et al. (2013, 2019). Kapsch et al. (2013, 2019) establishes a link between observed extremely low September Arctic pan-Arctic sea ice area and an anomalous early melt onset due to the footprint

of an anomalous cloudy and moist atmosphere on the net longwave radiative fluxes.

In order to trace back the net radiative flux anomalies to anomalous atmospheric conditions, we subdivide the net shortwave and longwave radiative surface fluxes into their downward and upward components (Fig. 8a, b). Strongly enhanced downward longwave radiation occurs between late winter and late spring, which is partly balanced by enhanced upward longwave radiation in accordance with anomalously high (near-)surface air temperatures during that period (cf. Figs. 6a–e and 8a). In June–July and July–August, positive downward radiative flux anomalies are much smaller than in spring, but counteracting upward longwave radiative flux anomalies drop to zero because sea ice-snow melting constraints surface temperatures to be close to the freezing point. In August–September, weakly enhanced upward and downward longwave radiative flux anomalies compensate each other. Regarding the shortwave radiative fluxes, reduced downward fluxes are overcompensated by reduced upward fluxes, leading to an anomalous net accumulation of energy in the snow-sea ice-ocean system due to shortwave fluxes between April–May and August–September (Fig. 8b).

The combination of enhanced downward longwave and reduced downward shortwave radiation suggests that extremely low sea ice summers are characterized by enhanced cloudiness. During extremely low sea ice summers, statistically significant positive cloud cover anomalies are present from late winter to late spring (Fig. 8c). The enhanced cloud cover is accompanied by positive integrated water vapour anomalies being statistically significant from late winter to mid-summer (Fig. 8c). Consequently, apart from anomalously high air temperatures, enhanced cloudiness and water vapour in the atmosphere contribute to the positive downward and net longwave radiative surface fluxes during extremely low sea ice summers. Reduced upward shortwave radiative fluxes are naturally emerging due the reduction in the downward shortwave radiative fluxes. However, a strongly reduced surface albedo due to reduced sea ice cover, i.e. the sea ice-albedo feedback, likewise contributes to the accumulation of energy related to the reduced upward shortwave fluxes (Fig. 8d).

4 Discussion and conclusions

The present study demonstrates the applicability of a rare event algorithm to improve the sampling efficiency of extremely low pan-Arctic sea ice area during the melting season. The simulations with the rare event algorithm produce several hundreds of times more extremes than the control run for the same computational cost, and allow us to compute return times of extremes two to three orders of magnitude larger than feasible with direct sampling. Owing
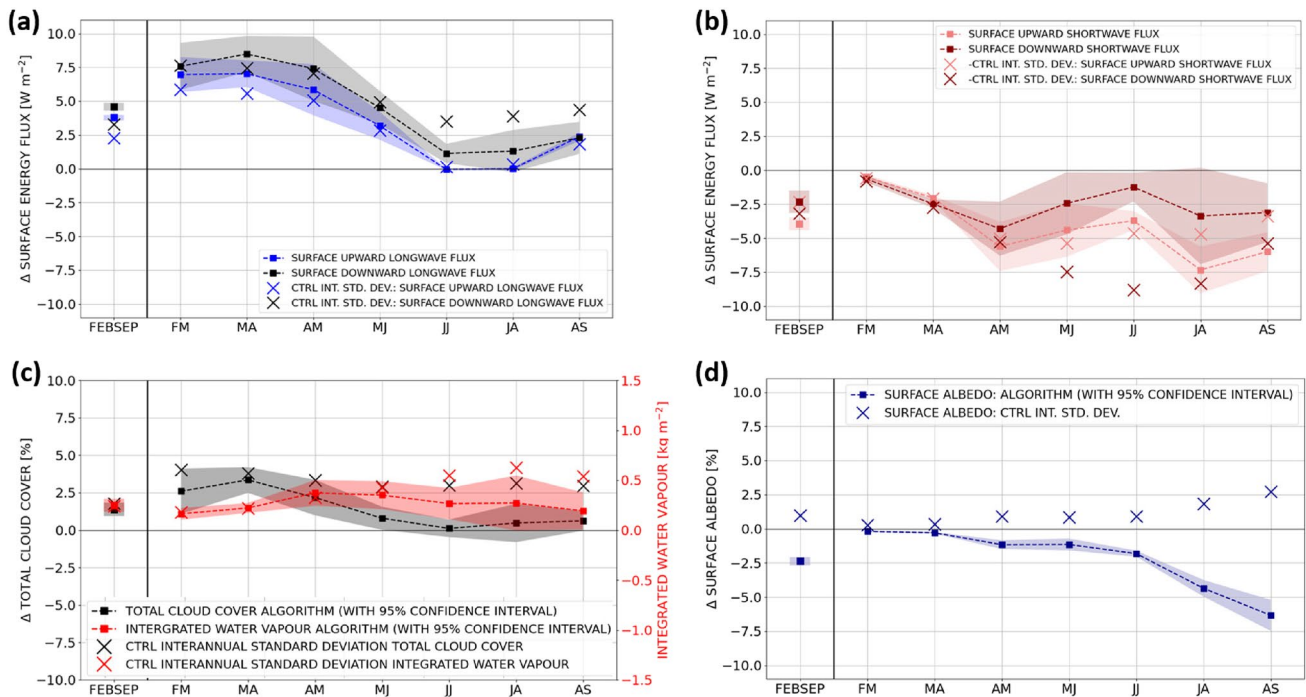
Fig. 8 Rare event algorithm experiments with a resampling time of $\tau_r = 5$ days: February–September and bimonthly mean domain-averaged anomalies of different variables conditional on extreme negative February–September mean pan-Arctic sea ice area anomalies equal or smaller than -2.5 standard deviations of the control ensembles. Mean anomalies are presented as an average over the five rare event algorithm experiments and are evaluated relative to the control run. Shading indicates 95% confidence intervals obtained from the statistics of the five estimates (see Supplementary Information S1). The domain is defined as in Fig. 7. Surface upward and downward **a** longwave and **b** shortwave radiative flux anomalies. Direction-independent absolute values of the downward and upward fluxes are considered, i.e., a positive (negative) anomaly indicates a radiative flux that is stronger (weaker) in magnitude than the climatology. **c** (black) Total cloud cover [%] and (red) integrated water vapour [kg m^{-2}] and **d** surface albedo [%] anomalies. **a**–**d** The "x" markers indicate respectively the climatological standard deviations in the control run

to the rare event algorithm, we compute statistically significant composites of dynamical quantities conditional on the occurrence of extremely low sea ice summers with return times of more than 200 years. In this way, we identify four processes and conditions that lead to extreme negative February–September mean pan-Arctic sea ice area anomalies in PlaSim-LSG: (1) preconditioning through the winter sea ice-ocean state, (2) enhanced downward longwave radiation due to an anomalously moist and warm Arctic atmosphere in spring, (3) enhanced downward sensible heat fluxes in May-June and (4) the sea ice-albedo feedback becoming active throughout late spring and summer.

The preconditioning manifests in large negative winter pan-Arctic sea ice volume anomalies as a result of both negative sea ice area and sea ice thickness anomalies (Fig. 5 and Supplementary Fig. S4a, b). The preconditioning of anomalously low summer pan-Arctic sea ice area through negative winter sea ice thickness anomalies is in agreement with Chevallier and Salas-Mélia (2012), Holland et al. (2011) and Kauker et al. (2009), who emphasize the important role of winter-spring sea ice thickness for the probability of sea ice to survive the melt season. Chevallier and Salas-Mélia

(2012) further argues that the winter-spring sea ice thickness, in particular the area covered by sea ice thicker than a critical thickness, is a better predictor of the summer pan-Arctic sea ice area than the winter-spring sea ice area itself. Anomalous states in the winter–spring sea ice thickness and sea ice area can be generated by a variety of mechanisms, including the dynamical forcing of the atmospheric circulation on the sea ice (e.g. Ogi et al. 2016; Rigor et al. 2002), mechanisms related to the sea ice memory itself (Blanchard-Wrigglesworth et al. 2011) and an anomalous heat content in the ocean (Polyakov et al. 2012; Comiso 2012). While a future study is required to examine the precise cause of the preconditioning in PlaSim-LSG, direct dynamical causes can be excluded due to the fact that a purely thermodynamic sea ice model is used in the present work.

The second process is related to an anomalously moist and warm atmosphere, which manifests in enhanced downward longwave radiation between February–March and July–August accompanied by enhanced downward sensible heat flux in May–June. Enhanced spring downward longwave radiation as one driver of extremely low summer Arctic sea ice area is consistent with Kapsch et al. (2013, 2019),

who demonstrate a linkage between observed extremely low September pan-Arctic sea ice area and a persistent anomalously moist and cloudy atmosphere in the preceding spring. Kapsch et al. (2019) and Persson (2012) argue that enhanced downward longwave radiation in spring can lead to enhanced surface warming prior to the melt onset and to an earlier melt onset compared to climatology. Kapsch et al. (2013, 2019) further demonstrate that the observed anomalously moist spring atmosphere prior to extremely low September Arctic sea ice area is related to enhanced meridional water vapour transport. In PlaSim-LSG, the anomalously moist and warm atmosphere may both be a trigger, i.e. via enhanced meridional heat and water vapour transport into the Arctic, and a response of extreme negative sea ice area anomalies, i.e. due to enhanced evaporation and sensible heat loss from the Arctic Ocean to the atmosphere due to positive surface temperature and open water fraction anomalies.

The third process suggests that the atmosphere may act not only as an amplifier but also as a trigger of sea ice retreat. In May–June, enhanced downward sensible heat fluxes over the Arctic Ocean are associated with a reinforcement of positive 500 hPa geopotential height anomalies compared to earlier months, while positive T2M anomalies are decreasing in amplitude (cf. Figs. 6 and 7c). Consequently, the positive 500 hPa geopotential height anomalies and thus the anomalously warm lower troposphere during the spring-summer transition cannot be explained alone by a diabatic forcing through an anomalously warm surface. The atmospheric dynamics and energy fluxes in May–June are compatible with the characteristics of midlatitude heatwaves. The possible role of Arctic heatwaves as drivers of extreme sea ice retreat is relatively understudied in the literature, and a detailed analysis of their impacts and dynamical origin will be subject of a future study.

The fourth process is given by the sea ice-albedo feedback, which sets in during April–May as a consequence and amplifier of extremely low sea ice cover. Compared to the different atmosphere-surface flux components discussed in Sect. 3.3, the sea ice-albedo feedback explains the largest amount of anomalous Arctic Ocean net energy accumulation during extremely low sea ice summers. Future rare event algorithm simulations with a prescribed surface albedo are a possibility to quantify the relative contribution of the sea ice-albedo feedback to extreme negative pan-Arctic sea ice area anomalies.

Overall, two reasons let us conclude that, in PlaSim-LSG, the preconditioning through the winter-spring sea ice-ocean state is a more dominant driver of extreme negative February–September mean pan-Arctic sea ice area anomalies than the anomalous atmospheric conditions. Firstly, pan-Arctic sea ice volume anomalies prior to extremely low sea ice summers are about one and a half standard deviations away from the climatology (Fig. 5b), while anomalies of

atmospheric quantities and of downward atmosphere-surface energy fluxes are mostly less than one standard deviation away from the climatology (Figs. 7c and 8a–c). Secondly, the most extreme February–September mean sea ice area anomalies obtained with the 5-days resampling time experiments only have marginally larger amplitudes than the ones obtained with the 30-days resampling time experiments (Fig. 3). Consequently, the targeted sampling of atmospheric drivers of sea ice reduction that act on the upper range of synoptic and on submonthly time scales do not substantially increase the magnitude of the most extreme sea ice area anomalies compared to the 30-days resampling time experiments, which are primarily designed to efficiently sample oceanic drivers of low sea ice states. We highlight, however, that this study is based on a relatively low resolution climate model with a purely thermodynamic sea ice model. A direct dynamic forcing of the atmospheric circulation on the sea ice, e.g., related to synoptic-scale storms or to the AO and the AD pattern, are therefore not captured by the model.

We point out that, even though the experiments with the rare event algorithm presented in this paper are designed to improve the sampling efficiency of February–September mean pan-Arctic sea ice area anomalies, the method indirectly also oversamples trajectories characterized by negative anomalies of the pan-Arctic sea ice area during the annual sea ice minimum in September (Fig. 2a, b; note that the correlation coefficient between FEBSEP and September (SEP) pan-Arctic sea ice area in the control run is 0.69). This suggests a potential applicability of the rare event algorithm to study extremes of the annual Arctic sea ice minimum. This could also be obtained by changing the observable used to weight the trajectories from the pan-Arctic sea ice area to its time derivative. Finally, we highlight that in the experiments presented in this paper the initial conditions of the ensemble have been taken from the control run in order to have an unbiased sampling of the invariant measure of the dynamics. In this way, the return times and statistics computed with the algorithm are related to unconditional probability distributions. A different type of experiment would consist in starting each ensemble member from the same initial condition, as done for ensemble weather and seasonal climate predictions. In this case, the algorithm would give access to the statistics of extreme events conditional on the chosen initial condition. This approach could be of great interest in the context of seasonal predictions in order to estimate the risk of observing a record low of Arctic sea ice in summer given the conditions at the beginning of the melting season. This strategy and the extent to which the accuracy of statistical estimators based on the importance sampling formula in these type of experiments improves the results compared to direct sampling constitute an exciting line of research that will be explored in future works.

Declarations

References

Alekseev G, Kuzmina S, Bobylev L et al (2019) Impact of atmospheric heat and moisture transport on the Arctic warming. Int J Climatol 39(8):3582–3592. https://doi.org/10.1002/joc.6040

Andres HJ, Tarasov L (2019) Towards understanding potential atmospheric contributions to abrupt climate changes: characterizing changes to the north atlantic eddy-driven jet over the last deglaciation. Clim Past 15(4):1621–1646. https://doi.org/10.5194/cp-15-1621-2019

Angeloni M (2022) Climate variability in an Earth system Model of Intermediate Complexity: from interannual to centennial timescales. PhD thesis, Università di Bologna, available at http://amsdottorato.unibo.it/10152/1/plasim.pdf

Arakawa A, Lamb VR (1977) Computational design of the basic dynamical process of the UCLA general circulation model. Methods Comp Phys 17:173–265

Årthun M, Eldevik T, Smedsrud LH et al (2012) Quantifying the influence of Atlantic heat on Barents Sea Ice variability and retreat. J Clim 25(13):4736–4743. https://doi.org/10.1175/JCLI-D-11-00466.1

Baldwin MP, Stephenson DB, Thompson DWJ et al (2003) Stratospheric memory and skill of extended-range weather forecasts. Science 301(5633):636–640. https://doi.org/10.1126/science.1087143

Blanchard-Wrigglesworth E, Armour KC, Bitz CM et al (2011) Persistence and inherent predictability of Arctic sea ice in a GCM ensemble and observations. J Clim 24(1):231–250. https://doi.org/10.1175/2010JCLI3775.1

Bouchet F, Marston JB, Tangarife T (2018) Fluctuations and large deviations of Reynolds stresses in zonal jet dynamics. Phys Fluids 30(1):015110. https://doi.org/10.1063/1.4990509

Chevallier M, Salas-Mélia D (2012) The role of sea ice thickness distribution in the Arctic sea ice potential predictability: a diagnostic approach with a coupled GCM. J Clim 25(8):3025–3038. https://doi.org/10.1175/JCLI-D-11-00209.1

Chripko S, Msadek R, Sanchez Gomez E et al (2021) Impact of Reduced Arctic Sea Ice on northern hemisphere climate and weather in autumn and winter. J Clim 34(14):5847–5867. https://doi.org/10.1175/JCLI-D-20-0515.1

Cini M, Zappa G, Ragone F et al (2024) Simulating AMOC tipping driven by internal climate variability with a rare event algorithm. npj Clim Atmos Sci 7(31):1–10. https://doi.org/10.1038/s41612-024-00568-7

Coles S (2001) An introduction to statistical modelling of extreme values. Springer-Verlag, London

Comiso JC (2012) Large decadal decline of the Arctic multiyear ice cover. J Clim 25(4):1176–1193. https://doi.org/10.1175/JCLI-D-11-00113.1

Del Moral P (2004) Feynman–Kac formulae genealogical and interacting particle systems with applications. Springer, New York

Del Moral P, Garnier J (2005) Genealogical particle analysis of rare events. Ann Appl Probab 15(4):2496–2534. https://doi.org/10.1214/105051605000000566

Delhaye S, Fichefet T, Massonnet F et al (2022) Summertime changes in climate extremes over the peripheral Arctic regions after a sudden sea ice retreat. Weather Clim Dyn Discuss 3(2):1–30. https://doi.org/10.5194/wcd-3-555-2022

Ding Q, Schweiger A, L'Heureux M et al (2017) Influence of high-latitude atmospheric circulation changes on summertime Arctic sea ice. Nat Clim Change 7(4):289–295. https://doi.org/10.1038/NCLIMATE3241

Drijfhout SS, Maier Reimer E, Mikolajewicz U (1996) Tracing the conveyor belt in the Hamburg large-scale geostrophic ocean general circulation model. J Geophys Res: Oceans 101(C10):22563–22575. https://doi.org/10.1029/96JC02162

Eicken H (2013) Arctic sea ice needs better forecasts. Nature 497(7450):431–433. https://doi.org/10.1038/497431a

Eliassen E, Machenhauer B, Rasmusson E (1970) On a numerical method for integration of the hydrodynamical equations with a spectral representation of the horizontal fields—Inst. of Theor. Met., Univ. Copenhagen https://doi.org/10.13140/RG.2.2.13894.88645

EUMETSAT Ocean and Sea Ice Satellite Application Facility (2017) Global sea ice concentration climate data record 1979-2015, v2p0, OSI-450, https://doi.org/10.15770/EUM_SAF_OSI_0008. ftp://osisaf.met.no/reprocessed/ice/conc/v2p0. Accessed 06 Jan 2023

EUMETSAT Ocean and Sea Ice Satellite Application Facility (2023) Sea Ice Index 1979–2022, v2p1, OSI-420, Norwegian Meteorological Institute. ftp://osisaf.met.no/prod_test/ice/index/v2p1/nh/osisaf_nh_sie_daily.nc. Accessed 06 Jan 2023

Fetterer F, Knowles K, Meier WN, et al (2017) Sea Ice Index, Version 3. National Snow and Ice Data Center, Boulder, CO, digital media. https://doi.org/10.7265/N5K072F8

Fischer EM, Beyerle U, Bloin-Wibe L et al (2023) Storylines for unprecedented heatwaves based on ensemble boosting. Nat Commun 14(1):4643. https://doi.org/10.1038/s41467-023-40112-4

Fraedrich K, Jansen H, Kirk E et al (2005) The Planet Simulator: towards a user friendly model. Meteorol Z 14(3):299–304. https://doi.org/10.1127/0941-2948/2005/0043

Francis JA, Vavrus SJ (2012) Evidence linking Arctic amplification to extreme weather in mid-latitudes. Geophys Res Lett. https://doi.org/10.1029/2012GL051000

Francis JA, Wu B (2020) Why has no new record-minimum Arctic sea-ice extent occurred since September 2012? Environ Res Lett 15(11):114034. https://doi.org/10.1088/1748-9326/abc047

Francis JA, Chan W, Leathers DJ et al (2009) Winter Northern Hemisphere weather patterns remember summer Arctic sea ice extent. Geophys Res Lett. https://doi.org/10.1029/2009GL037274

Gessner C, Fischer EM, Beyerle U et al (2023) Developing low-likelihood climate storylines for extreme precipitation over central Europe. Earth's Future 11(9):e2023EF003628. https://doi.org/10.1029/2023EF003628

Giardina C, Kurchan J, Lecomte V et al (2011) Simulating rare events in dynamical processes. J Stat Phys 145(4):787–811. https://doi.org/10.1007/s10955-011-0350-4

Grafke T, Vanden-Eijnden E (2019) Numerical computation of rare events via large deviation theory. Chaos 29(6):063118. https://doi.org/10.1063/1.5084025

Grafke T, Grauer R, Schäfer T (2015) The instanton method and its numerical implementation in fluid mechanics. J Phys A: Math Theor 48(33):333001. https://doi.org/10.1088/1751-8113/48/33/333001

Gregory JM, Stott PA, Cresswell DJ et al (2002) Recent and future changes in Arctic sea ice simulated by the HadCM3 AOGCM. Geophys Res Lett. https://doi.org/10.1029/2001GL014575

Guemas V, Doblas Reyes F, Germe A et al (2013) September 2012 Arctic sea ice minimum: discriminating between sea ice memory, the August 2012 extreme storm, and prevailing warm conditions [in Explaining Extreme Events of 2012 from a Climate Perspective]. Bull Am Meteorol Soc 94(9):S20–S22

Hertwig E, Lunkeit F, Fraedrich K (2014) Low-frequency climate variability of an aquaplanet. Theoret Appl Climatol 121:459–478. https://doi.org/10.1007/s00704-014-1226-8

Holland MM, Bailey DA, Vavrus S (2011) Inherent sea ice predictability in the rapidly changing Arctic environment of the Community Climate System Model, version 3. Clim Dyn 36:1239–1253. https://doi.org/10.1007/s00382-010-0792-4

Hoven VDI (1957) Power spectrum of horizontal wind speed in the frequency range from 0.0007 to 900 cycles per hour. J Atmos Sci 14(2):160–164. https://doi.org/10.1175/1520-0469(1957)014<0160:PSOHWS>2.0.CO;2

Jungclaus JH, Koenigk T (2010) Low-frequency variability of the arctic climate: the role of oceanic and atmospheric heat transport variations. Clim Dyn 34:265–279. https://doi.org/10.1007/s00382-009-0569-9

Kahn H, Harris TE (1951) Estimation of particle transmission by random sampling. Natl Bur Stand Appl Math Ser 12:27–30

Kapsch ML, Graversen RG, Tjernström M (2013) Springtime atmospheric energy transport and the control of Arctic summer sea-ice extent. Nat Clim Change 3(8):744–748. https://doi.org/10.1038/NCLIMATE1884

Kapsch ML, Skific N, Graversen RG et al (2019) Summers with low Arctic sea ice linked to persistence of spring atmospheric circulation patterns. Clim Dyn 52:2497–2512. https://doi.org/10.1007/s00382-018-4279-z

Kauker F, Kaminski T, Karcher M et al (2009) Adjoint analysis of the 2007 all time Arctic sea-ice minimum. Geophys Res Lett 36(3):L03707. https://doi.org/10.1029/2008GL036323

Kuo HL (1965) On formations and intensification of tropical cyclone through latent heat release by cumulus convection. J Atmos Sci 22:40–63. https://doi.org/10.1175/1520-0469(1965)022<0040:OFAIOT>2.0.CO;2

Kuo HL (1974) Further studies of the parameterization of the influence of cumulus convection on large-scale flow. J Atmos Sci 31(5):1232–1240. https://doi.org/10.1175/1520-0469(1974)031<1232:FSOTPO>2.0.CO;2

Lacis AA, Hansen J (1974) A parameterization for the absorption of solar radiation in the Earth's atmosphere. J Atmos Sci 31(1):118–133. https://doi.org/10.1175/1520-0469(1974)031<0118:APFTAO>2.0.CO;2

Laursen L, Eliasen E (1989) On the effects of the damping mechanisms in an atmospheric general circulation model. Tellus 41A:385–400. https://doi.org/10.1111/j.1600-0870.1989.tb00390.x

Lawrence DM, Slater AG, Tomas RA et al (2008) Accelerated Arctic land warming and permafrost degradation during rapid sea ice loss. Geophys Res Lett. https://doi.org/10.1029/2008GL033985

Lestang T, Ragone F, Bréhier CE et al (2018) Computing return times or return periods with rare event algorithms. J Stat Mech: Theory Exp 4:043213. https://doi.org/10.1088/1742-5468/aab856

Lestang T, Bouchet F, Lévêque E (2020) Numerical study of extreme mechanical force exerted by a turbulent flow on a bluff body by direct and rare-event sampling techniques. J Fluid Mech 895:A19. https://doi.org/10.1017/jfm.2020.293

Lindsay RW, Zhang J, Schweiger A et al (2009) Arctic Sea Ice retreat in 2007 follows thinning trend. J Clim 22(1):165–176. https://doi.org/10.1175/2008JCLI2521.1

Lloyd's (2012) Arctic opening: opportunity and risk in the high north, C. House, eds. https://www.chathamhouse.org/sites/default/files/publications/0412arctic.pdf. Accessed 29 Mar 2022

Louis JF (1979) A parametric model of vertical eddy fluxes in the atmosphere. Bound Layer Meteorol 17(2):187–202. https://doi.org/10.1007/BF00117978

Louis JF, Tiedke M, Geleyn M (1981) A short history of the PBL parameterisation at ECMWF. In: Proceedings of the ECMWF Workshop on Planetary Boundary Layer Parameterization. Reading, pp 59–80

Lunkeit F, Borth H, Böttinger M, et al (2012) Planet Simulator: Reference Manual Version 16. Tech. rep., Meteorologisches Institut, Universität Hamburg

Maier-Reimer E, Mikolajewicz U (1992) The Hamburg Large Scale Geostrophic Ocean General Circulation Model Cycle 1. World Data Center for Climate (WDCC) at DKRZ https://doi.org/10.2312/WDCC/DKRZ_Report_No02

Maier-Reimer E, Mikolajewicz U, Hasselmann K (1993) Mean circulation of the Hamburg LSG OGCM and its sensitivity to the thermohaline surface forcing. J Phys Oceanogr 23(4):731–757. https://doi.org/10.1175/1520-0485(1993)023<0731:MCOTHL>2.0.CO;2

Mehling O, Bellomo K, Angeloni M et al (2023) High-latitude precipitation as a driver of multicentennial variability of the AMOC in a climate model of intermediate complexity. Clim Dyn 61(3–4):1519–1534. https://doi.org/10.1007/s00382-022-06640-3

Notz D, Marotzke J (2012) Observations reveal external driver for Arctic sea-ice retreat. Geophys Res Lett 39(8):1–6. https://doi.org/10.1029/2012GL051094

Ogi M, Rysgaard S, Barber DG (2016) Importance of combined winter and summer Arctic Oscillation (AO) on September sea ice extent. Environ Res Lett 11(3):034019

Ono J, Tatebe H, Komuro Y (2019) Mechanisms for and predictability of a drastic reduction in the Arctic Sea Ice: APPOSITE data with Climate Model MIROC. J Clim 32(5):1361–1380. https://doi.org/10.1175/JCLI-D-18-0195.1

Orszag SA (1970) Transform method for calculating of vector coupled sums. J Atmos Sci 27:890–895. https://doi.org/10.1175/1520-0469(1970)027<0890:tmftco>2.0.co;2

Overland JE, Francis JA, Hanna E et al (2012) The recent shift in early summer Arctic atmospheric circulation. Geophys Res Lett 39(19):L19804. https://doi.org/10.1029/2012GL053268

Parey S, Hoang TTH, Dacunha Castelle D (2010) Different ways to compute temperature return levels in the climate change context. Environmetrics 21(7–8):698–718. https://doi.org/10.1002/env.1060

Parkinson CL, Comiso J (2013) On the 2012 record low Arctic sea ice cover: combined impact of preconditioning and an August storm. Geophys Res Lett 40(7):1356–1361. https://doi.org/10.1002/grl.50349

Persson POG (2012) Onset and end of the summer melt season over sea ice: thermal structure and surface energy perspective from SHEBA. Clim Dyn 39:1349–1371. https://doi.org/10.1007/s00382-011-1196-9

Petoukhov V, Semenov VA (2010) A link between reduced Barents–Kara sea ice and cold winter extremes over northern continents. J Geophys Res Atmos. https://doi.org/10.1029/2009JD013568

Petrie RE, Shaffrey LC, Sutton RT (2015) Atmospheric response in summer linked to recent Arctic sea ice loss. Q J R Meteorol Soc 141(691):2070–2076. https://doi.org/10.1002/qj.2502

Plotkin DA, Webber RJ, O'Neill ME et al (2019) Maximizing simulated tropical cyclone intensity with action minimizing. J Adv Model Earth Syst 11(4):863–891. https://doi.org/10.1029/2018ms001419

Polyakov IV, Walsh JE, Kwok R (2012) Recent changes of arctic multiyear sea ice coverage and the likely causes. Bull Am Meteorol Soc 93(2):145–151. https://doi.org/10.1175/BAMS-D-11-00070.1

Ragone F, Bouchet F (2020) Computation of extreme values of time averaged observables in climate models with large deviation techniques. J Stat Phys 179(5):1637–1665. https://doi.org/10.1007/s10955-019-02429-7

Ragone F, Bouchet F (2021) Rare event algorithm study of extreme warm summers and heatwaves over Europe. Geophys Res Lett 48(12):e2020GL091197. https://doi.org/10.1029/2020GL091197

Ragone F, Wouters J, Bouchet F (2018) Computation of extreme heat waves in climate models using a large deviation algorithm. Proc Natl Acad Sci 115(1):24–29. https://doi.org/10.1073/pnas.1712645115

Rigor IG, Wallace JM, Colony RL (2002) Response of sea ice to the Arctic oscillation. J Clim 15(18):2648–2663. https://doi.org/10.1175/1520-0442(2002)015<2648:ROSITT>2.0.CO;2

Sasamori T (1968) The radiative cooling calculation for application to general circulation experiments. J Appl Meteorol Climatol 7(5):721–729. https://doi.org/10.1175/1520-0450(1968)007<0721:TRCCFA>2.0.CO;2

Sauer J, Ragone F, Massonnet F et al (2023) Supplementary materials for extremes of summer arctic sea ice reduction investigated with a rare event algorithm. Zenodo. https://doi.org/10.5281/zenodo.8414273

Schweiger AJ, Zhang J, Lindsay RW et al (2008) Did unusually sunny skies help drive the record sea ice minimum of 2007? Geophys Res Lett. https://doi.org/10.1029/2008GL033463

Screen JA, Simmonds I (2010) The central role of diminishing sea ice in recent Arctic temperature amplification. Nature 464(7293):1334–1337. https://doi.org/10.1038/nature09051

Screen JA, Deser C, Smith DM et al (2018) Consistency and discrepancy in the atmospheric response to Arctic sea-ice loss across climate models. Nat Geosci 11(3):155–163. https://doi.org/10.1038/s41561-018-0059-y

Semtner AJ (1976) A model for the thermodynamic growth of sea ice in numerical investigations of climate. J Phys Oceanogr 6:379–389

Serreze MC, Barry RG (2014) The Arctic climate system. In: Houghton JT, Rycroft MJ, Dessler AJ (eds) Cambridge atmospheric and space science series. Cambridge University Press, Cambridge

Serreze MC, Francis JA (2006) The Arctic amplification debate. Clim Change 76:241–264. https://doi.org/10.1007/s10584-005-9017-y

Slingo A, Slingo JM (1991) Response of the National Center for Atmospheric Research community climate model to improvements in the representation of clouds. J Geophys Res 96(D8):15341–15357. https://doi.org/10.1029/91JD00930

Smith LC, Stephenson SR (2013) New Trans-Arctic shipping routes navigable by midcentury. Proc Natl Acad Sci 110(13):E1191–E1195. https://doi.org/10.1073/pnas.1214212110

Stephens GL, Paltridge GW, Platt C (1978) Radiation profiles in extended water clouds. III: observations. J Atmos Sci 35(11):2133–2141. https://doi.org/10.1175/1520-0469(1978)035<2133:RPIEWC>2.0.CO;2

Stephens GL, Ackermann S, Smith EA (1984) A shortwave parameterization revised to improve cloud absorption. J Atmos Sci 41(4):687–690. https://doi.org/10.1175/1520-0469(1984)041<0687:ASPRTI>2.0.CO;2

Stroeve J, Notz D (2018) Changing state of Arctic sea ice across all seasons. Environ Res Lett 13(10):1–23. https://doi.org/10.1088/1748-9326/aade56

Swaluw VDE, Drijfhout SS, Hazeleger W (2007) Bjerknes compensation at high northern latitudes: the ocean forcing the atmosphere. J Clim 20(24):6023–6032. https://doi.org/10.1175/2007JCLI1562.1

Wang J, Zhang J, Watanabe E et al (2009) Is the Dipole Anomaly a major driver to record lows in Arctic summer sea ice extent? Geophys Res Lett 36(5):L05706. https://doi.org/10.1029/2008GL036706

Webber RJ, Plotkin DA, O'Neill ME et al (2019) Practical rare event sampling for extreme mesoscale weather. Chaos 29(5):053109. https://doi.org/10.1063/1.5081461

Woodgate RA, Weingartner T, Lindsay R (2010) The 2007 Bering Strait oceanic heat flux and anomalous Arctic sea-ice retreat. Geophys Res Lett 37(1):L01602. https://doi.org/10.1029/2009GL041621

Wouters J, Schiemann RKH, Shaffrey LC (2023) Rare event simulation of extreme European winter rainfall in an intermediate complexity climate model. J Adv Model Earth Syst 15(4):e2022MS003537. https://doi.org/10.1029/2022MS003537

Zhang J, Lindsay R, Steele M et al (2008) What drove the dramatic retreat of arctic sea ice during summer 2007? Geophys Res Lett 35(11):L11505. https://doi.org/10.1029/2008GL034005

Zhang J, Lindsay R, Schweiger A et al (2013) The impact of an intense summer cyclone on 2012 Arctic sea ice retreat. Geophys Res Lett 40(4):720–726. https://doi.org/10.1002/grl.50190